

DFT based comparative analysis of physical properties of binary metallic diborides XB_2 (X = Cr, Mo and W)

Razu Ahmed^{1,2}, Md. Sohel Rana¹, Md. Sajidul Islam¹, S. H. Naqib^{1*}

¹Department of Physics, University of Rajshahi, Rajshahi-6205, Bangladesh

²Department of Physics, Bangladesh Army University of Engineering and Technology, Qadirabad-6431, Bangladesh

*Corresponding author, Email: salehnaqib@yahoo.com

Abstract

Transition-metal borides (TMBs) have long attracted attention of the researchers because of their unique mechanical and electrical properties including superconductivity. We have explored the structural, mechanical, electronic, optical, and some thermophysical properties of XB_2 (X = Cr, Mo and W) binary metallic diborides in detail employing density functional theory based first-principles method. Many of the physical properties, including direction-dependent mechanical properties, optical properties, and thermo-mechanical properties are being investigated for the first time. According to this study, XB_2 (X = Cr, Mo and W) compounds exhibit reasonably good machinability, delocalized metallic bonding, and high Vickers hardness with high Debye temperature. CrB_2 and MoB_2 exhibit brittleness whereas WB_2 show ductility. The mechanical stability of XB_2 (X = Cr, Mo and W) compounds has been confirmed. Based on the calculated bulk modulus, Young's modulus and shear modulus of XB_2 (X = Cr, Mo and W) compounds can be regarded as potential candidates of ultra-incompressible and hard materials. The metallic nature of XB_2 (X = Cr, Mo and W) compounds is confirmed via electronic band structures with a high electronic energy density of states at the Fermi level. The optical parameters exhibit excellent agreement with the electrical properties. All optical constants show a considerable degree of anisotropy. The reflectivity spectra reveal that XB_2 (X = Cr, Mo and W) compounds are good reflectors in the infrared and near-visible regions. The compounds under study have a high Debye temperature, melting temperature, lattice thermal conductivity, and minimum phonon thermal conductivity, which corresponds well to their elastic and bonding properties. The extremely high melting temperature of WB_2 indicates that WB_2 is a promising material for high-temperature applications. The superconducting state parameters of XB_2 (X = Cr, Mo and W) compounds are also investigated.

Keywords: Density functional theory; Metallic diborides; Thermo-mechanical properties; Optoelectronic properties; Superconductivity

1. Introduction

Transition-metal borides (TMBs) have a wide range of practical uses due to their unique physical properties such as large bulk modulus, high hardness, ultrahigh melting points, favorable thermal stability, strong resistance to oxidation, excellent electric transport properties, and superconductivity at high temperature [1–3]. These have great potential for application in harsh

environments such as those encountered by hypersonic flight, scramjet and rocket propulsion, atmospheric re-entry, hard coatings for electromechanical systems, armor, and cutting tools [1–5].

In addition to the fascinating chemical properties already described, metal diborides also take on distinct crystal structures based on the R_M/R_B ratio, where R_M and R_B are atomic radii of metallic and boron atoms, respectively. The most representative category of TMBs is generated by the layered hexagonal diborides with AlB_2 -type structure which features a graphitelike boron layer alternated with a close-packed metal layer [6,7]. Strong B–B bonds in the boron layer provide structural stability. The range of the R_M/R_B ratio for these stable AlB_2 -like TMB phases is 1.14 to 2.06 [8,9]. Superhard ReB_2 has a hexagonal structure with a unique zigzag network generated by the strong Re–B and B–B bonds [6,10] which contributes significantly to its high hardness. However, subsequent experiments identified that the structure of XB_2 ($X = Cr, Mo$ and W) should have an AlB_2 -type structure ($P6/mmm$, No. 191) [11–13].

The surprising discovery of superconductivity in magnesium diboride (MgB_2) with superconducting transition temperature $T_c \sim 39$ K has provided a fresh and strong impetus for research into this family of materials [14 - 18]. Superconductivity has also been observed in OsB_2 ($T_c = 2.1$ K) and RuB_2 ($T_c = 1.6$ K) [16,17]. The electron-phonon interaction is the driving force behind the observed superconductivity in each of these compounds, which show the wide range of material types and applications that include B-B bonds and metals. According to theoretical calculations [19,20], superconductivity of MoB_2 in the MgB_2 type structure at high pressure still falls within the traditional BCS-type. Furthermore, the compound CrB_2 demonstrates superconductivity at a transition temperature of up to 7 K when external pressure is applied, but superconductivity of CrB_2 is detected when the antiferromagnetic transition at $T_N \sim 88$ K is totally suppressed under ambient pressure [21].

In the present work, we employed first-principles calculations based on the density functional theory (DFT) to investigate the crystal structures of XB_2 ($X = Cr, Mo$ and W) compounds. Some earlier experimental and theoretical findings on the selected materials were reported in Refs. [11–13,22,23]. However, there is still a noticeable lack of information on these materials. This lack of information reduces the viability of its possible applications. To the best of our knowledge, many important physical properties (e.g., elastic, optoelectronic, and thermo-physical properties) have yet to be studied. Additionally, the mechanical anisotropy characterized by the direction dependence of the shear modulus, Young's modulus, linear compressibility, and Poisson's ratio of CrB_2 and WB_2 compounds has not been discussed at all, except for MoB_2 [17].

In this study, we conducted a comparative analysis of the physical properties of XB_2 ($X = Cr, Mo$ and W) compounds in order to completely grasp their structural, elastic, electronic, optical, thermo-mechanical, and superconducting state properties. The results obtained are compared with those found in previous studies where available. When selecting a system for applications involving optoelectronic devices, optical properties are crucial to understand. The behavior of a material at various temperatures may be inferred from thermo-physical properties. Mechanical anisotropy is crucial for understanding key mechanical behaviors such as crack formation and its subsequent propagation, crystal structure instability, phase transformation, and growth of plastic deformations which sometimes restrict efficient applications of materials. Additionally, this

study computes bond hardness, fracture toughness, and brittleness index, which are useful for designing any part of a structure or device. a comprehensive understanding of the elastic, mechanical, thermomechanical, and optical response of these compounds is necessary to unravel the full promise of XB_2 ($X = \text{Cr, Mo and W}$) for potential applications. This constitutes the primary motivation of the present study.

The rest of the paper is organized as follows: In Section 2, we have discussed the computational scheme. Section 3 reveals the computational results and analyses. Finally, the major findings of this study are discussed and summarized in Section 4.

2. Computational scheme

Ground state study of the systems is performed with the Kohn-Sham density functional theory (KS-DFT) [24] using the CAmbridge Serial Total Energy Package (CASTEP) code [25]. The generalized gradient approximation (GGA) with Perdew–Burke–Ernzerhof (PBE) [26], and local density approximation (LDA) [27,28] have been employed for the exchange-correlation functionals. Optimized geometry is obtained using GGA (PBE) for CrB_2 and LDA for MoB_2 and WB_2 . Ultrasoft Vanderbilt-type pseudopotentials [29] have been employed to model the electron-ion interactions and represent electronic wavefunctions using a plane wave basis set [30]. We treated $[3s^23p^63d^54s^1]$, $[4s^24p^64d^55s^1]$, $[5s^25p^65d^46s^2]$, and $[2s^22p^1]$ as valence electron configurations for Cr, Mo, W, and B atoms, respectively. In this paper, Monkhorst-Pack grid of k -point meshes with the sizes of $12 \times 12 \times 10$ for CrB_2 and WB_2 , and $21 \times 21 \times 18$ for MoB_2 have been selected and the cut-off energy for the plane wave expansion is set to 550 eV. The BFGS (Broyden-Fletcher-Goldfarb-Shanno) algorithm [31] was used as the minimization algorithm, and density mixing was used to determine the electronic structure. The convergence criterion of relaxation on the lattice unit cell has been kept within a limit of 5×10^{-6} eV-atom⁻¹ for energy, 0.01 eV Å⁻¹ for maximum force, 0.02 GPa for maximum stress, and 5×10^{-4} Å for maximum atomic displacement.

The elastic constants, C_{ij} , are acquired from the stress-strain relationship [32]. The Voigt-Reuss-Hill (VRH) method [33,34] is used to estimate all the other polycrystalline elastic parameters, including the bulk modulus (B), shear modulus (G), and Young's modulus (Y) and Poisson ratio (σ).

The energy/frequency dependent complex dielectric function, $[\varepsilon(\omega) = \varepsilon_1(\omega) + i\varepsilon_2(\omega)]$, can be used to obtain all the optical parameters. CASTEP uses the following expression to calculate the frequency dependent imaginary part of the dielectric function:

$$\varepsilon_2(\omega) = \frac{2e^2\pi}{\Omega\varepsilon_0} \sum_{k,v,c} |\langle \psi_k^c | \hat{u} \cdot \vec{r} | \psi_k^v \rangle|^2 \delta(E_k^c - E_k^v - E) \quad (1)$$

where, Ω is the cell volume, ω is the angular frequency of incident electromagnetic wave (EMW), \hat{u} is the unit vector giving the polarization direction of the electric field, e is the electronic charge, ψ_k^c and ψ_k^v are the conduction and valence band wave functions at a fixed wave-vector k . The delta function in Equation (1) ensures energy and momentum conservation during the optical transition. The well-known Kramers-Kronig equation links the real and imaginary components of $\varepsilon(\omega)$:

$$\varepsilon_1(\omega) = 1 + \frac{2}{\pi} P \int_0^{\infty} \frac{\omega' \varepsilon_2(\omega') d\omega'}{(\omega'^2 - \omega^2)} \quad (2)$$

In Equation (2), P signifies the principal part of the dielectric function. All the other important optical parameters including absorption coefficient [$\alpha(\omega)$], optical conductivity [$\sigma(\omega)$], loss function [$L(\omega)$], reflectivity [$R(\omega)$], and refractive index [real, $n(\omega)$, and imaginary, $k(\omega)$, parts], are estimated from the dielectric function $\varepsilon(\omega)$. The interrelations are given below [35–39]:

$$\alpha(\omega) = \frac{4\pi k(\omega)}{\lambda} \quad (3)$$

$$n(\omega) = \frac{1}{\sqrt{2}} [\{\varepsilon_1(\omega)^2 + \varepsilon_2(\omega)^2\}^{1/2} + \varepsilon_1(\omega)]^{1/2} \quad (4)$$

$$k(\omega) = \frac{1}{\sqrt{2}} [\{\varepsilon_1(\omega)^2 + \varepsilon_2(\omega)^2\}^{1/2} - \varepsilon_1(\omega)]^{1/2} \quad (5)$$

$$R(\omega) = \left| \frac{\tilde{n} - 1}{\tilde{n} + 1} \right| = \frac{(n - 1)^2 + k^2}{(n + 1)^2 + k^2} \quad (6)$$

$$\sigma(\omega) = \frac{2W_{cv}\hbar\omega}{\tilde{E}_0^2} \quad (7)$$

$$L(\omega) = \text{Im}\left(-\frac{1}{\varepsilon(\omega)}\right) \quad (8)$$

In Equation (7), W_{cv} is the photon induced optical transition probability per unit time.

3. Results and discussions

3.1 Structural

The compound XB_2 ($X = \text{Cr, Mo and W}$) conforms to an AlB_2 -type layered structure with a space group of $\text{P6}/mmm$ (No. 191) [11–13,15]. Figure 1 shows the schematic crystal structure of XB_2 ($X = \text{Cr, Mo and W}$). It is a simple hexagonal lattice of close-packed metal layers alternating with graphite-like B layers perpendicular to the c direction [15,40]. With three closest neighbor B atoms in each plane, the boron atoms are positioned at the corners of a hexagon. The metal atoms are found in the center of the B hexagons, midway between adjacent boron layers. One metal and two atoms of boron make up the primitive cell. There is one metal and one B in nonequivalent atomic positions of X (0, 0, 0) and B (1/3, 2/3, 1/2) [11–13,15].

The optimized structural parameters of XB_2 ($X = \text{Cr, Mo and W}$) are shown in Table 1 along with the experimental and theoretical results [11–13,22] for comparison. The computed lattice parameters are in excellent agreement with the experimental results. The calculated ratios c/a for each of the XB_2 phases is also presented in Table 1. Pearson's criteria states [15,41] that for stable AlB_2 -like phases, the ratio c/a should fall between 0.59 and 1.2. Thus, from the data obtained it may be concluded that the XB_2 ($X = \text{Cr, Mo and W}$) for which $c/a < 1.2$, should be stable, whereas WB_2 ($c/a = 1.12$) is close to the upper limit of stability.

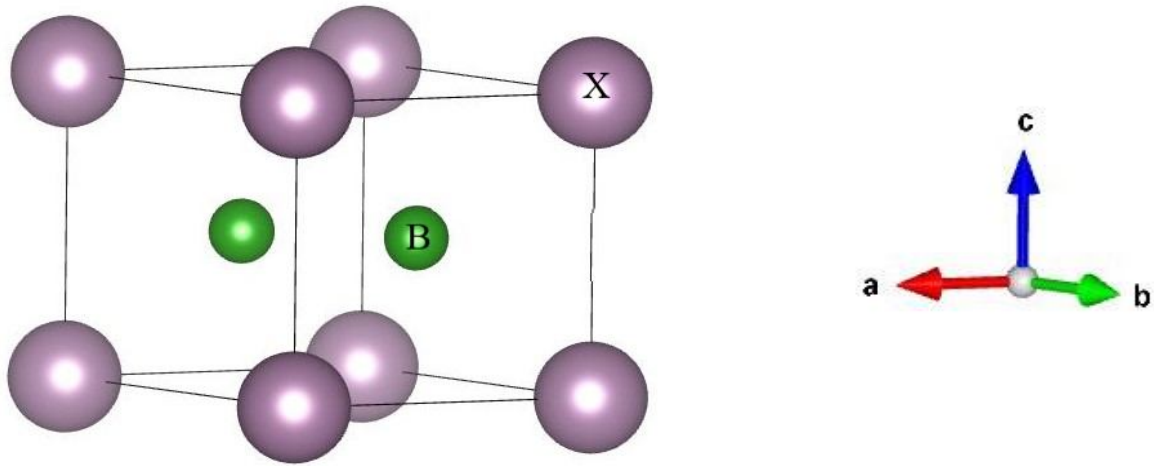


Figure 1. Schematic crystal structure of XB_2 ($\text{X} = \text{Cr}, \text{Mo}$ and W). Crystallographic axes are shown on the right.

Table 1: Calculated lattice constants a , b and c (all in \AA), equilibrium volume V_0 (\AA^3), number of formula units in the unit cell Z and total number of atoms in the unit cell N of XB_2 ($\text{X} = \text{Cr}, \text{Mo}$ and W) compounds.

Compound	a	b	c	c/a	V_0	Z	N	Reference
CrB_2	2.97	2.97	2.94	0.99	22.49	1	3	This work
	2.98	2.98	3.07	-	23.50	1	3	[11] ^{Expt.}
MoB_2	2.99	2.99	3.28	1.09	25.38	1	3	This work
	3.05	3.05	3.07	-	24.67	1	3	[12] ^{Expt.}
	3.01	3.01	3.31	1.10	-	-	-	[15] ^{Theo.}
WB_2	2.97	2.97	3.32	1.12	25.43	1	3	This work
	3.02	3.02	3.05	-	24.09	1	3	[13] ^{Expt.}
	3.05	3.05	3.31	-	26.69	1	3	[22] ^{Theo.}

3.2 Elastic properties

In order to predict a material's response to external stresses, it is necessary to comprehend the majority of its solid-state properties, including brittleness, ductility, stiffness, structural stability,

normal modes of oscillations, elastic wave propagation, and anisotropy. The values of five independent elastic constants (C_{ij} , namely C_{11} , C_{12} , C_{13} , C_{33} , and C_{44}) of XB_2 ($X = \text{Cr, Mo and W}$) phases are summarized in Table 2. Mechanically stable phases should satisfy the well-known Born criteria [15,42,43] applicable to hexagonal structure:

$$C_{11} > 0, C_{44} > 0, (C_{11} - C_{12}) > 0, (C_{11} + C_{12})C_{33} - 2C_{12}^2 > 0 \quad (9)$$

All the elastic constants of XB_2 ($X = \text{Cr, Mo and W}$) are positive and satisfy the above-mentioned criteria. This implies that XB_2 ($X = \text{Cr, Mo and W}$) compounds are mechanically stable.

The elastic tensors C_{11} and C_{33} signify the elastic stiffness of crystals against the strains along the principal axes (the crystallographic a- and c-directions, respectively). The difference between C_{11} and C_{33} implies that crystals are elastically anisotropic. In this view, the elastic anisotropy level in CrB_2 is more than that of MoB_2 and WB_2 . The low value of C_{44} indicates the shearability of the compounds. Of the three compounds studied here, WB_2 is the most resistant to shear deformation while the CrB_2 is the most shearable one. Additionally, the indentation hardness of materials is associated with the elastic tensor C_{44} . The indentation hardness increases with C_{44} . Thus, of the three phases discussed here, WB_2 is expected to be the hardest.

Table 2: Calculated elastic constants C_{ij} of XB_2 ($X = \text{Cr, Mo and W}$) compounds (all in GPa).

Compound	C_{11}	C_{12}	C_{13}	C_{33}	C_{44}	Reference
CrB_2	559.90	120.79	166.03	309.62	126.20	This work
	583.70	117.30	119.30	343.30	143.10	[24]
MoB_2	645.33	138.52	242.09	453.44	177.62	This work
	613.00	120.00	220.00	391.00	168.00	[12]
	621.40	116.90	228.40	404.30	175.00	[15]
WB_2	717.28	256.20	330.88	668.87	202.14	This work
	590.10	187.40	236.40	442.80	98.80	[23]

The Hill approximated values of bulk modulus (B_H) and shear modulus (G_H) (using the Voigt-Reuss-Hill (VRH) method) [44–47], Young's modulus (Y), Poisson's ratio (σ), Lamé constants (μ , λ), Tetragonal shear modulus (C'), Cauchy pressure, (C''), machinability index (μ_M), Kleinman parameter (ξ) of XB_2 ($X = \text{Cr, Mo and W}$) have been computed using the following standard formulae [15,46,48–54]:

$$B_H = \frac{B_V + B_R}{2} \quad (10)$$

$$G_H = \frac{G_V + G_R}{2} \quad (11)$$

$$Y = \frac{9BG}{(3B + G)} \quad (12)$$

$$\sigma = \frac{(3B - 2G)}{2(3B + G)} \quad (13)$$

$$\mu = \frac{Y}{2(1 + \sigma)} \quad (14)$$

$$\lambda = \frac{\sigma Y}{(1 + \sigma)(1 - 2\sigma)} \quad (15)$$

$$C' = \frac{C_{11} - C_{12}}{2} \quad (16)$$

$$C'' = (C_{12} - C_{44}) \quad (17)$$

$$\mu_M = \frac{B}{C_{44}} \quad (18)$$

$$\zeta = \frac{C_{11} + 8C_{12}}{7C_{11} + C_{12}} \quad (19)$$

The results obtained are presented in Table 3 and Table 4. Table 3 shows that $B > G$, which implies that the shearing stress should determine the mechanical stability of XB_2 ($X = \text{Cr, Mo}$ and W) compounds and the shape deforming stress, as opposed to the volume altering stress, will dictate the mechanical failure mechanism of XB_2 ($X = \text{Cr, Mo,}$ and W) compounds. The value of Y represents a material's stiffness (resistance to length change) [55,56]. Higher Young's modulus corresponds to increased stiffness of a material. Moreover, greater values of Young's modulus indicate a higher degree of covalency in a material [57]. The tetragonal shear modulus of a crystal is the measure of crystal's stiffness and its positive value suggests the dynamical stability of the solid. Therefore, it is anticipated that the compounds being studied will be dynamically stable.

Table 3: Bulk modulus B and shear modulus G (both in Voigt-Reuss-Hill (VRH) method), Young's modulus Y , tetragonal shear modulus C' and Cauchy pressure C'' of XB_2 ($X = \text{Cr, Mo}$ and W) compounds (all in GPa).

Compound	B_V	B_R	B	G_V	G_R	G	Y	C'	C''	Reference
CrB_2	259.46	244.76	252.11	159.50	143.02	151.26	378.15	219.56	-5.41	This work

	-	-	240.00	-	-	175.00	422.50	-	-	[23]
MoB ₂	332.17	329.77	330.97	196.49	181.69	189.09	476.52	253.41	-39.10	This work
	-	-	304.00	-	-	186.00	463.00	-	-	[12]
WB ₂	437.71	437.55	437.63	205.99	202.87	204.43	530.67	230.54	54.06	This work
	327.00	324.10	325.60	144.00	129.50	136.70	359.70	-	-	[22]

Some of the indicators that are used to determine whether a solid is brittle or ductile include the Pugh's ratio (B/G), Poisson's ratio (σ), and Cauchy pressure (C''). The critical value of Pugh's ratio is 1.75 [58,59], Poisson's ratio is 0.26 [60], and Cauchy pressure is zero [51,53]. If the values of C'' are positive (negative), σ is higher (lower) than 0.26, and B/G is larger (lesser) than 1.75, the material is considered ductile (brittle) [38,61]. The calculated values of these parameters, which are shown in Table 3 and Table 4, suggest that CrB₂ and MoB₂ are brittle whereas WB₂ is ductile.

The Poisson ratio (σ) defines the relationship between lateral and axial strain caused by an applied axial stress [17,62]. For solids with central force dominance, the value of σ ranges from 0.25 to 0.50 [63]. For XB₂, the values of σ vary from 0.25–0.30, suggesting that the interatomic force is the central in type. In simple terms, the value of σ for covalent materials is around 0.10 and $G \sim 1.1B$; for ionic materials, it is usually about 0.25 and $G \sim 0.6B$; and for metallic materials, it is usually about 0.25 or more and $G \sim 0.4B$ [64]. In our case the values of σ for XB₂ vary from about 0.25–0.30, indicating the delocalized metallic bonding should be dominant for the diborides. We have also calculated the Lamé constants. In terms of physical properties, the first Lamé constant, λ indicates the compressibility of the material while the second Lamé constant, μ reflects its shear stiffness [15].

The property of a material that determines how readily a cutting tool may be used to machine it is referred to as its "machinability". In today's industry, knowing a solid's machinability is crucial since it determines the best possible machine usage, cutting forces, temperature, and plastic strain. This indicator can also be used to test a solid's plasticity and dry lubricating properties [65–67]. A high value of machinability index (μ_M) suggests greater ease of shape manipulation, lower feed forces, excellent dry lubricating properties, lower friction value, and higher plastic strain value. The values of machinability index of XB₂ indicate that they possess high level of machinability. The compounds also have a notable amount of dry lubricity.

The Kleinman parameter (ζ), commonly known as the internal strain parameter, measures a substance's ability to bend and stretch. The value of ζ typically varies from 0 to 1 [49]. The lower and higher limits of ζ signify the noteworthy role of bond stretching/contracting and bond bending to resist external force, respectively. The calculated values of ζ of XB₂ indicate that the bond stretching contribution dominates in WB₂, MoB₂ and CrB₂.

Table 4: Pugh's indicator or ratio B/G , Kleinman parameter ζ , Poisson's ratio σ , Lamé constants (μ, λ), and machinability index μ_M of XB_2 ($X = Cr, Mo$ and W) compounds.

Compound	B/G	ζ	σ	μ	λ	μ_M	Reference
CrB ₂	1.67	0.37	0.25	151.26	151.26	2.00	This work
	-	-	0.20	-	199.60	-	[15,23]
MoB ₂	1.75	0.38	0.26	189.09	204.85	1.86	This work
	-	-	0.28	-	241.80	-	[15]
WB ₂	2.14	0.50	0.30	204.10	306.16	2.16	This work
	-	-	0.32	-	324.30	-	[15,22]

Table 4 presents the findings from earlier theoretical research [15,22,23]. Very good agreement with the calculated parameters is found.

Hardness is defined as the resistance of a material to local deformation induced by pressing a harder solid (indenter). From the standpoint of the application, the material's hardness is crucial. C_{44} and G are considered to be the best elastic constant and modulus for predicting the hardness of solids [68]. Hardness can be characterized theoretically by various schemes. X. Chen *et al.* (H_{macro}) [69], Y. Tian *et al.* [$(H_V)_{Tian}$] [70], and D. M. Teter [$(H_V)_{Teter}$] [71] developed hardness formulae based on either G or both G and B , whereas the formulae developed by N. Miao *et al.* (H_{micro}) [72] and E. Mazhnik *et al.* [$(H_V)_{Mazhnik}$] [73] are based on the Young's modulus and Poisson's ratio. The values of H_{micro} , H_{macro} , $(H_V)_{Tian}$, $(H_V)_{Teter}$, and $(H_V)_{Mazhnik}$ have been calculated using the following equations:

$$H_{micro} = \frac{(1 - 2\sigma)Y}{6(1 + \sigma)} \quad (20)$$

$$H_{macro} = 2\left[\left(\frac{G}{B}\right)^2 G\right]^{0.585} - 3 \quad (21)$$

$$(H_V)_{Tian} = 0.92(G/B)^{1.137} G^{0.708} \quad (22)$$

$$(H_V)_{Teter} = 0.151G \quad (23)$$

$$(H_V)_{Mazhnik} = \gamma_0 \chi(\sigma) Y \quad (24)$$

In Equation (24), $\chi(\sigma)$ is a function of the Poisson's ratio and can be evaluated from:

$$\chi(\sigma) = \frac{1 - 8.5\sigma + 19.5\sigma^2}{1 - 7.5\sigma + 12.2\sigma^2 + 19.6\sigma^3}$$

where γ_0 is a dimensionless constant with a value of 0.096. The discrepancy in hardness values obtained is due to the varied parameters used in equations (20) - (24). The obtained values are disclosed in Table 5. It appears that all the studied compounds possess high level of hardness.

In heavy-duty equipment, the formation of cracks is one of the most significant issues with the surface hard coatings, particularly in ceramic and metal materials. A solid's resistance to the initiation of cracks or fractures is measured by its fracture toughness, or K_{IC} . K_{IC} has been evaluated using the following formula [74]:

$$K_{IC} = \alpha_0^{-1/2} V_0^{1/6} [\xi(\sigma)Y]^{3/2} \quad (25)$$

where V_0 = volume per atom; $\alpha_0 = 8840$ GPa (for covalent and ionic crystals); $\xi(\sigma)$ is a parameter depending on the Poisson's ratio (σ), which can be found from:

$$\xi(\sigma) = \frac{1 - 13.7\sigma + 48.6\sigma^2}{1 - 15.2\sigma + 70.2\sigma^2 - 81.5\sigma^3}$$

As presented in Table 5, the values of K_{IC} of the XB_2 ($X = Cr, Mo$ and W) are 3.28, 5.38, and 5.13 $MPam^{1/2}$, respectively. It is evident that MoB_2 provides the best resistance against the formation and propagation of surface cracks. This result agrees with the computed hardness value.

Table 5: Calculated hardness (GPa) based on elastic moduli and Poisson's ratio and fracture toughness K_{IC} ($MPam^{1/2}$) of XB_2 ($X = Cr, Mo$ and W) compounds.

Compound	$(H_V)_{Micro}$	$(H_V)_{macro}$	$(H_V)_{Tian}$	$(H_V)_{Teter}$	$(H_V)_{Mazhnik}$	K_{IC}	Reference
CrB_2	25.21	17.73	17.98	22.84	17.43	3.28	This work
MoB_2	30.26	19.31	19.92	28.55	22.58	5.38	This work
	-	15.90	-	-	-	-	[12]
WB_2	27.54	15.45	16.74	30.87	27.67	5.13	This work
	26.50	-	-	-	-	-	[75]

The elastic anisotropy of crystal refers to a difference in the elastic responses upon loading along different directions. Additionally, elastic anisotropy influences the way in which microscale cracks in ceramics grow and propagate, as well as the mobility of charged defects, the alignment or misalignment of quantum dots, unusual phonon modes, plastic relaxation in thin films, and other elastic processes. The anisotropy levels of XB_2 ($X = Cr, Mo$ and W) are computed using the widely employed formulas.

For a hexagonal crystal, the shear anisotropy factor may be expressed in terms of three distinct parameters [76,77]. Taking into account the {100} shear planes between the <011> and <010> directions, the shear anisotropy factor, A_1 is as follows:

$$A_1 = \frac{4C_{44}}{C_{11} + C_{33} - 2C_{13}} \quad (26)$$

Taking into account the {010} shear plane between <101> and <001> directions the shear anisotropy factor, A_2 is as follows:

$$A_2 = \frac{4C_{55}}{C_{22} + C_{33} - 2C_{23}} \quad (27)$$

Taking into account the {001} shear planes between <110> and <010> directions, the anisotropy factor, A_3 is as follows:

$$A_3 = \frac{4C_{66}}{C_{11} + C_{22} - 2C_{12}} \quad (28)$$

The deviations of the factors A_1 , A_2 , and A_3 from unity reflect the crystal's elastic anisotropy for shape-changing deformation. Table 6 shows the calculated values for these anisotropy factors. The XB_2 (X = Cr, Mo, and W) compounds are predicted to be anisotropic based on the calculated values of A_1 , A_2 , and A_3 .

The elastic coefficients provide a method to evaluate the linear compressibility. The formula for defining the compressibility anisotropy coefficients k_c/k_a , which are specific to hexagonal crystals exclusively, is the ratio of the linear compressibility coefficient along the crystallographic c-axis to the linear compressibility coefficient along the crystallographic a-axis and can be expressed as [78]:

$$k_c/k_a = \frac{(C_{11} + C_{12} - 2C_{13})}{(C_{33} - C_{13})} \quad (29)$$

Deviation of k_c/k_a from unity determines the anisotropy level in linear compression. The k_c/k_a of CrB_2 , MoB_2 , and WB_2 is about 2.43, 1.42 and 0.92, respectively. These values suggested that the compressibility along the c-axis is much greater than the a-axis in CrB_2 and MoB_2 compounds while the compressibility along the c-axis is much smaller than the a-axis in WB_2 which agrees well with the calculated elastic constants along different axis shown in Table 2.

The universal log-Euclidean anisotropy index is defined as follows [79,80]:

$$A^L = \sqrt{[\ln(\frac{B_V}{B_R})]^2 + 5[\ln(\frac{C_{44}^V}{C_{44}^R})]^2} \quad (30)$$

In this scheme, the Voigt and Reuss values of C_{44} are calculated from [79]:

$$C_{44}^R = \frac{5}{3} \frac{C_{44}(C_{11} - C_{12})}{3(C_{11} - C_{12}) + 4C_{44}}$$

and

$$C_{44}^V = C_{44}^R + \frac{3(C_{11} - C_{12} - 2C_{44})^2}{5[3(C_{11} - C_{12}) + 4C_{44}]}$$

For perfect isotropy, $A^L = 0$. It is challenging to determine if a solid is layered or lamellar based solely on the value of A^L . Generally, large number (78%) of inorganic crystalline solids that have high A^L values, exhibit layered/lamellar structure [79]. Roughly, compounds with higher (lower) A^L values exhibit significant layered (non-layered) structural character. For the low values of A^L , XB_2 compounds are likely to have non-layered features.

The universal anisotropy index, (A^U, d_E) , equivalent Zener anisotropy measure, A^{eq} , percentage anisotropy in compressibility, A_B and anisotropy in shear, A_G (or A_C) for crystals are calculated from the following expressions [81–83]:

$$A^U = 5 \frac{G_V}{G_R} + \frac{B_V}{B_R} - 6 \geq 0 \quad (31)$$

$$d_E = \sqrt{A^U + 6} \quad (32)$$

$$A^{eq} = \left(1 + \frac{5}{12}A^U\right) + \sqrt{\left(1 + \frac{5}{12}A^U\right)^2 - 1} \quad (33)$$

$$A_B = \frac{B_V - B_R}{B_V + B_R} \quad (34)$$

$$A_G = \frac{G_V - G_R}{2G_H} \quad (35)$$

A unique way to quantify anisotropy that works for all crystal systems regardless of their symmetry is the universal anisotropy index, A^U . Isotropy is implied by $A^U = 0$, whereas anisotropy is shown by a nonzero value of A^U . Anisotropy is predicted for XB_2 (X = Cr, Mo and W) compounds based on the calculated values of A^U . On the other hand, equivalent Zener anisotropy measure, $A^{eq} = 1$, represents isotropy, while any other value suggests anisotropy. Table 6 displays the computed values of A^{eq} for XB_2 , which predicts that XB_2 are elastically anisotropic. Two anisotropy variables (A_B and A_G , respectively) that are proportionate to

anisotropy in compression and shear exist. The factors are called percentage anisotropy factors, and they provide zero values for crystals that are perfectly isotropic when taking shear and compression into account. The degree of anisotropy increases when the value increases from zero to a positive value. For XB_2 , anisotropy in shear is stronger than anisotropy in compressibility, as indicated by the larger value of A_G (Table 6) in comparison to A_B . Overall, it appears that CrB_2 is more anisotropic than MoB_2 and WB_2 . WB_2 is least anisotropic among the three.

Table 6: Shear anisotropy factors (A_1 , A_2 and A_3), linear compressibility coefficients k_c/k_a , universal log-Euclidean index A^L , universal anisotropy index A^U , equivalent Zener anisotropy measure A^{eq} , anisotropy in compressibility A^B (%), and anisotropy in shear A^G or A^C (%) of XB_2 ($X = \text{Cr, Mo and W}$) compounds.

Compound	A_1	A_2	A_3	k_c/k_a	A^L	A^U	A^{eq}	A^B	A^G	Layered/Non-layered
CrB_2	0.94	0.94	1.00	2.43	0.46	0.64	2.04	0.03	0.05	Non-layered
MoB_2	1.16	1.16	1.00	1.42	0.20	0.41	1.78	0.004	0.04	Non-layered
WB_2	1.12	1.12	1.00	0.92	0.03	0.08	1.29	0.002	0.008	Non-layered

We have analyzed and displayed the two-dimensional (2D) and three-dimensional (3D) profiles of the Young's modulus (Y), shear modulus (G), compressibility (β) (inverse of the bulk modulus), and Poisson's ratio (σ) of the XB_2 ($X = \text{Cr, Mo and W}$) compounds. These profiles were generated by ELATE [84]. Mechanically isotropic solids require 3D contour plots with spherical forms; otherwise, anisotropy exists. Figure 2 displays the 3D profiles of Y , β , G , and σ , all of which deviate from the spherical form, demonstrating anisotropy. ELATE also offers a numerical study, displaying the minimum and maximum values of each modulus, as well as the directions along which these extrema occur. The maximum and minimum values of Y , β , G , and σ , as well as their respective maximum to minimum ratios are disclosed in Table 7. These ratios are important in determining the elastic anisotropy in XB_2 . The anisotropy A_X of each elastic modulus X can be defined as follows [43,84]:

$$A_X = \begin{cases} X_{\text{max}}/X_{\text{min}} & \text{if } \text{sign}(X_{\text{max}}) = \text{sign}(X_{\text{min}}) \\ \infty & \text{otherwise.} \end{cases} \quad (36)$$

The anisotropy in Young's modulus, linear compressibility, shear modulus and Poisson's ratio are observed to be the lowest for WB_2 and highest for CrB_2 . The 2D plots depict the projections of 3D profiles onto the principal crystal planes. These plots show how the elastic properties exhibit anisotropy in various directions inside the specified crystal planes.

The plots for shear modulus and Poisson's ratio are complex due to their dependence on two orthogonal unit vectors in the direction of the measurement and the direction of applied stress [84,85]. Figures 4 and 5 show the 2D projections of shear modulus and Poisson's ratio,

with green (blue) lines representing the minimum (maximum) positive values of each property of the respective elastic parameters.

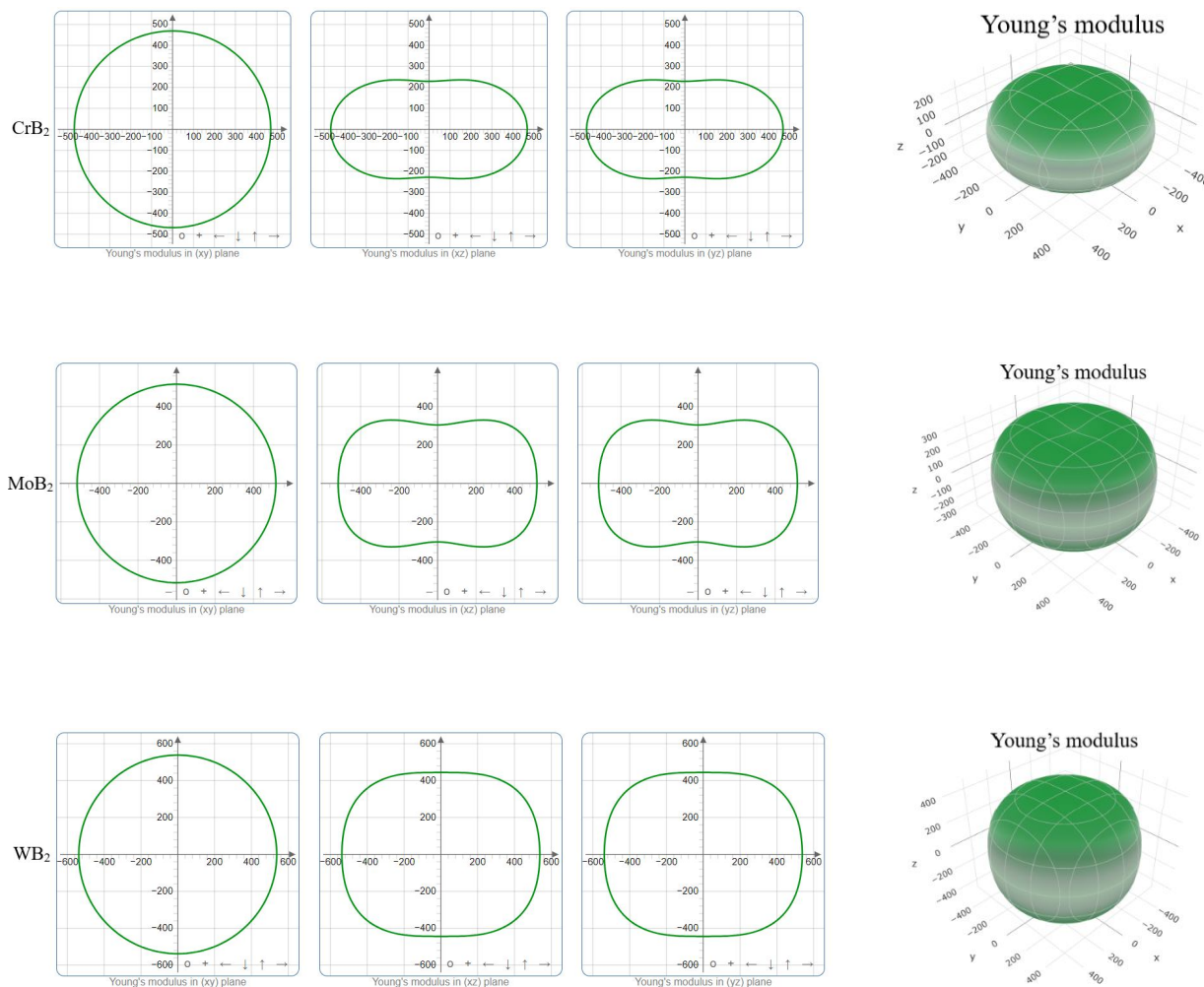


Figure 2. 2D (left) and 3D (right) directional dependences in Young's modulus (Y) of XB_2 compounds.

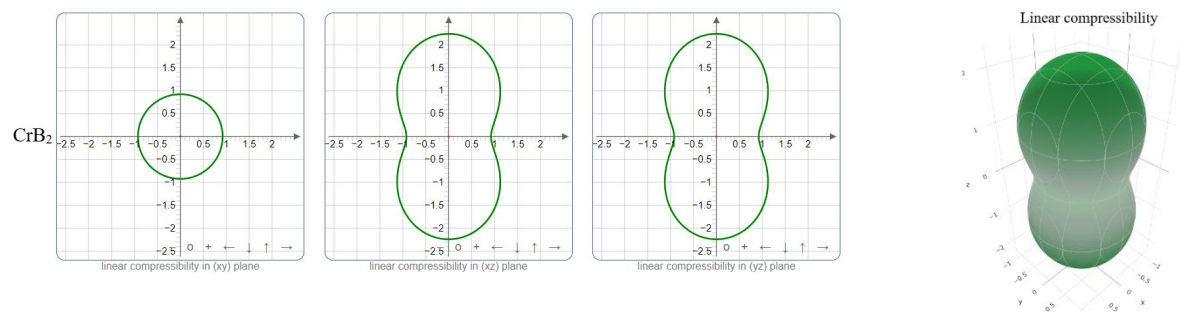
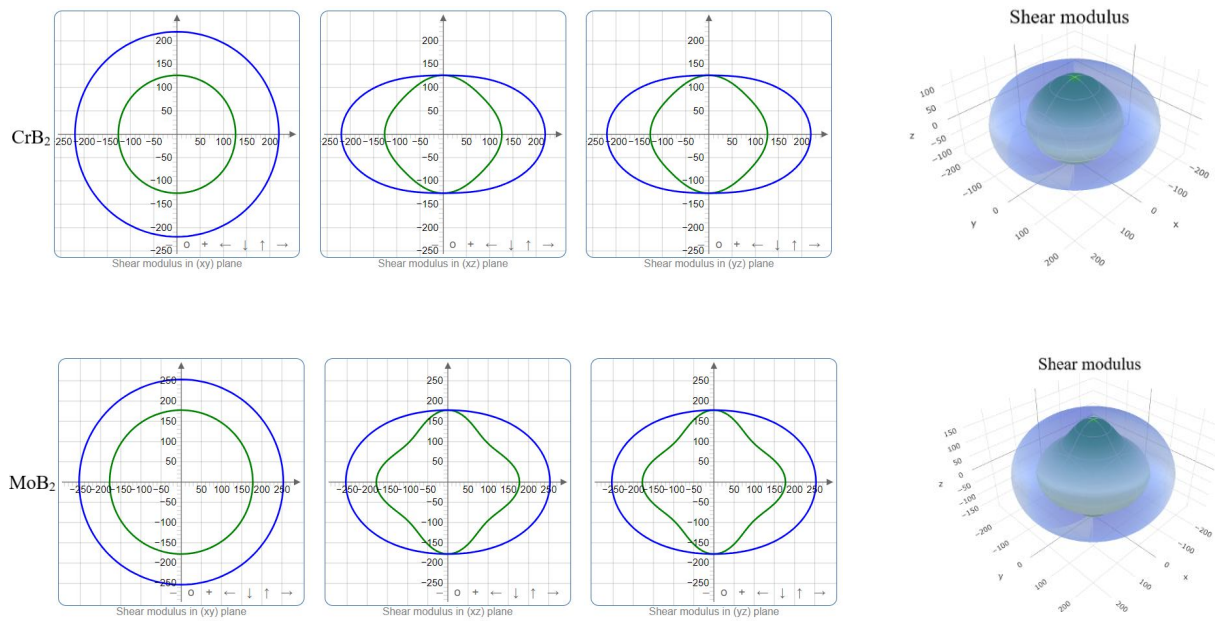




Figure 3. 2D (left) and 3D (right) directional dependences in compressibility (β) of XB_2 compounds.



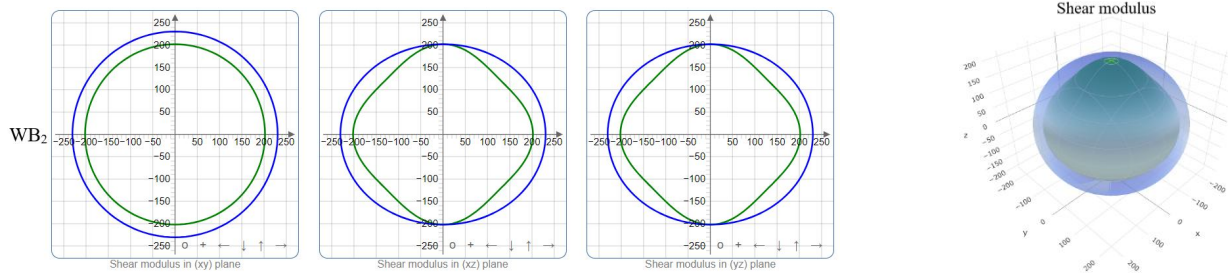


Figure 4. 2D (left) and 3D (right) directional dependences in shear modulus (G) of XB_2 compounds.

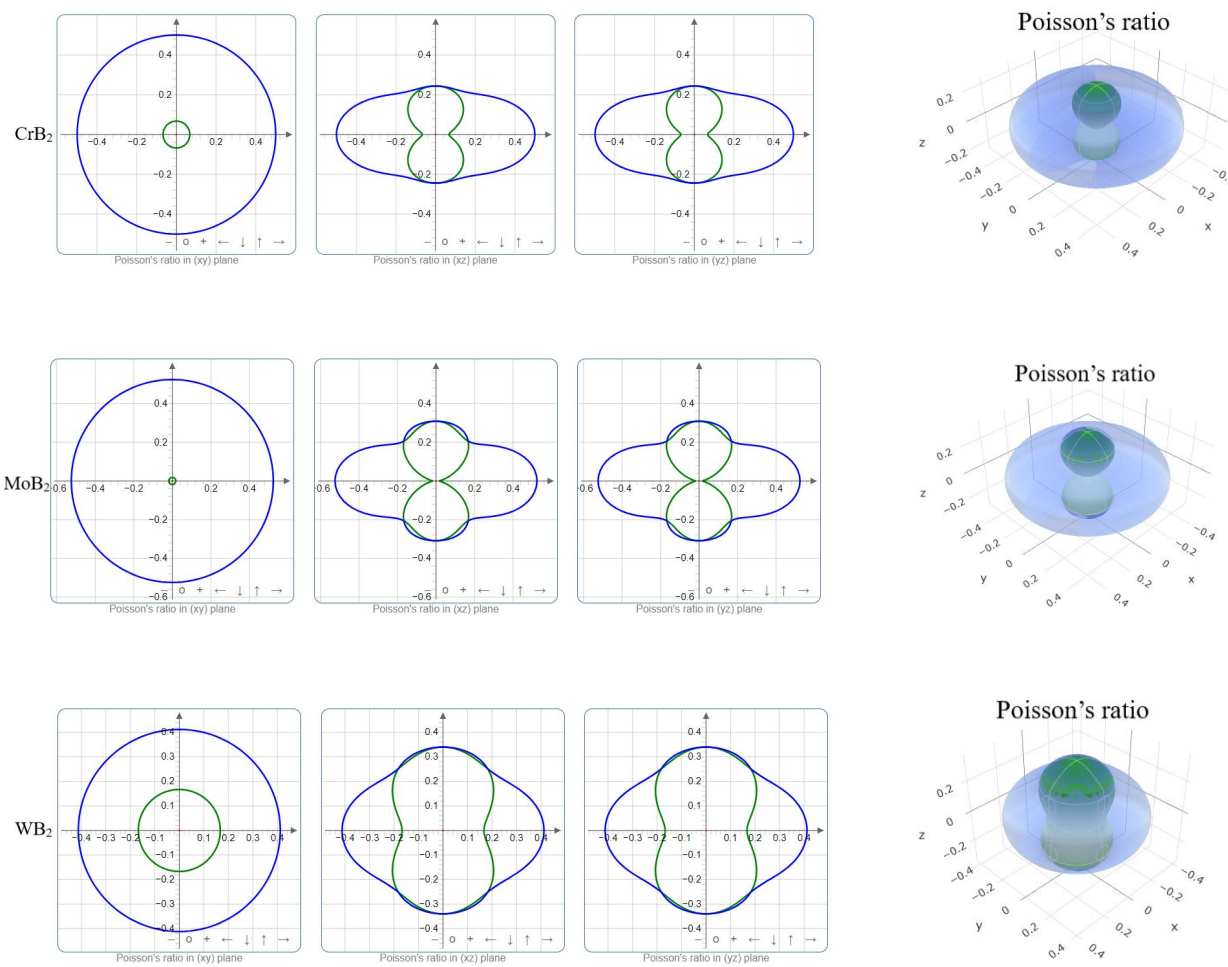


Figure 5. 2D (left) and 3D (right) directional dependences in Poisson's ratio (σ) of XB_2 compounds.

Table 7: The minimum and maximum values of Young's modulus (GPa), compressibility (TPa^{-1}), shear modulus (GPa), Poisson's ratio, and elastic anisotropies A_X ($X = Y, \beta, G, \sigma$) of XB_2 compounds.

Phase	Y		A_Y	β		A_β	G		A_G	σ		A_σ
	Y_{min}	Y_{max}		β_{min}	β_{max}		G_{min}	G_{max}		σ_{min}	σ_{max}	
CrB_2	228.63	468.73	2.05	0.92	2.24	2.43	115.73	219.56	1.89	0.07	0.50	7.41
MoB_2	303.90	519.11	1.71	0.89	1.26	1.42	137.71	253.41	1.84	0.02	0.52	29.21
WB_2	443.95	547.72	1.23	0.72	0.78	1.08	177.24	230.54	1.30	0.17	0.41	2.47

3.3 Electronic band structure and density of states

To understand the electronic and optical properties of XB_2 ($X = \text{Cr}, \text{Mo}$ and W) compounds, an investigation of the electronic band structure is essential. The behavior of electrons within the Brillouin zone (BZ) is determined by their energy dispersion $[E(k)]$. We have calculated the electronic band structure for the optimized crystal structures of XB_2 ($X = \text{Cr}, \text{Mo}$ and W) compounds along several high symmetry directions (Γ - M - K - Γ - A - L - H - A) in the first BZ. The Fermi level is indicated by the horizontal broken line placed at zero energy. As shown in Figure 6, no band gap exists in the band structures exhibiting the metallic character. The presence of highly dispersed bands leads in a low charge carrier effective mass [86–88] and a high charge mobility. The scenario is reversed for the non-dispersive bands. Overall, for all the three metallic diborides under investigation, the bands along L - H directions are less dispersive indicating relatively high effective mass and as a result, low mobility of charge carriers along this direction. Overall, the degree of dispersion in the bands crossing the Fermi level is higher for WB_2 compared to the other two metallic diborides.

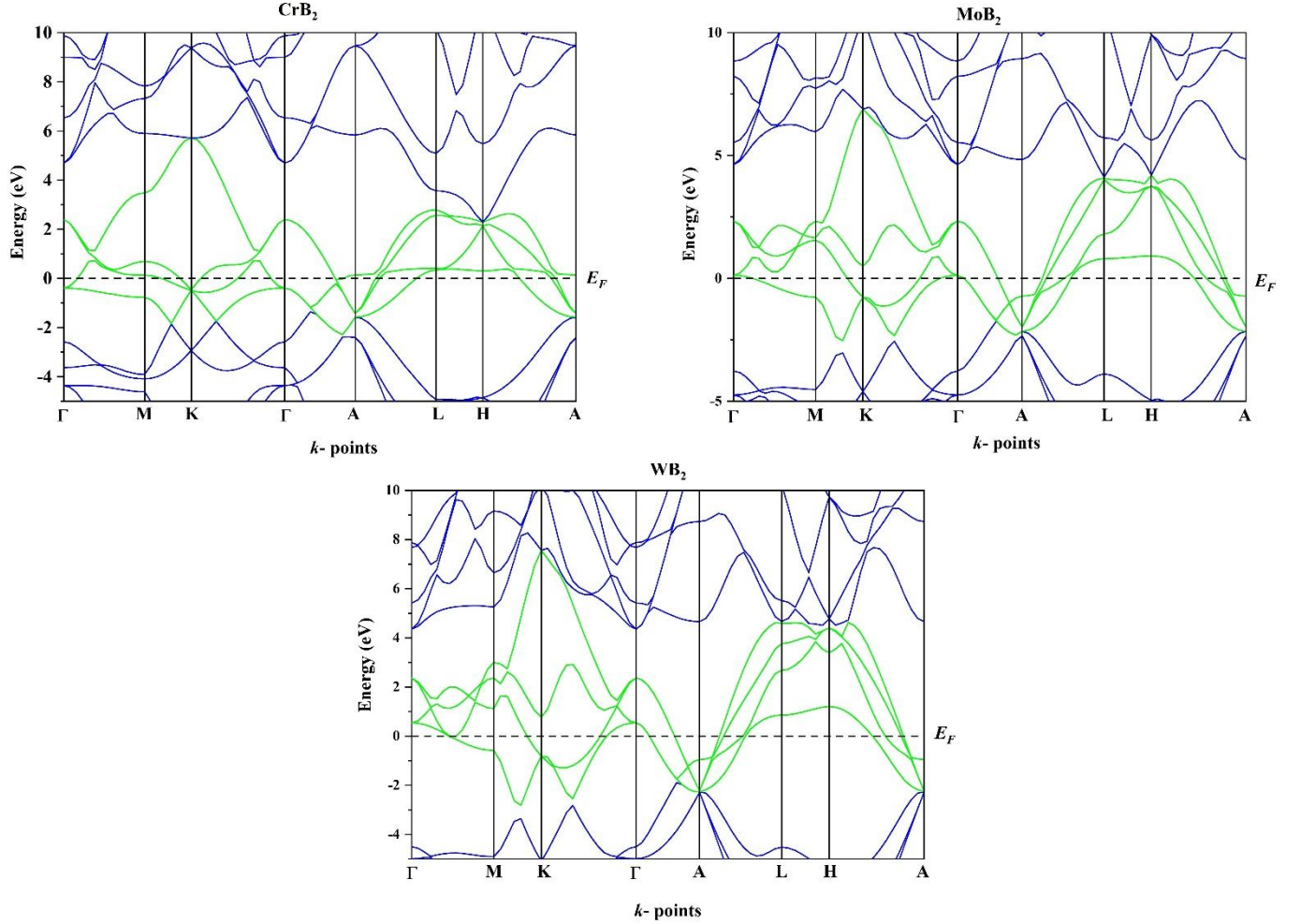


Figure 6. The band structures of XB_2 ($\text{X} = \text{Cr}, \text{Mo}$ and W) compounds in the first Brillouin zone.

To understand the electronic properties of these three materials on a fundamental level, the total and partial density of states (TDOSs and PDOSs, respectively) are illustrated in Figure 7 in which vertical dashed line at 0 eV represents the Fermi level, E_F . To investigate the contribution of different atoms to the TDOS, we have computed the PDOSs for Cr, Mo, W, and B in XB_2 ($\text{X} = \text{Cr}, \text{Mo}$ and W) compounds. At the Fermi level, the TDOSs for CrB_2 , MoB_2 , and WB_2 are 2.52, 1.34, and 1.25 electronic states per eV, respectively. As a result, of the three diborides, CrB_2 should have the highest conductivity. Close to the Fermi level, the main contribution to the TDOSs comes from the Cr-3d (84.92%) orbitals for CrB_2 , Mo-4d (74.18%) for MoB_2 , and W-5d (69.36%) for WB_2 . Thus, these electronic states should dominate the electrical conductivity of the XB_2 compounds. The properties of this electronic state also have an impact on the chemical and mechanical stabilities of XB_2 . The peaks, particularly those at the Fermi level, should influence charge flow and electrical transport properties. In the TDOS, the bonding peak is the nearest peak at the negative energy below the Fermi level, while the anti-bonding peak is the nearest peak at the positive energy above the Fermi energy. The energy gap between these peaks is called the pseudo-gap, which indicates electrical stability; crystals with more bonding electrons are structurally more stable [89,90]. In XB_2 compounds bonding and anti-bonding

peaks are located within 2.70 eV for CrB₂, 0.84 eV for MoB₂, and 0.81eV for WB₂ from the Fermi level.

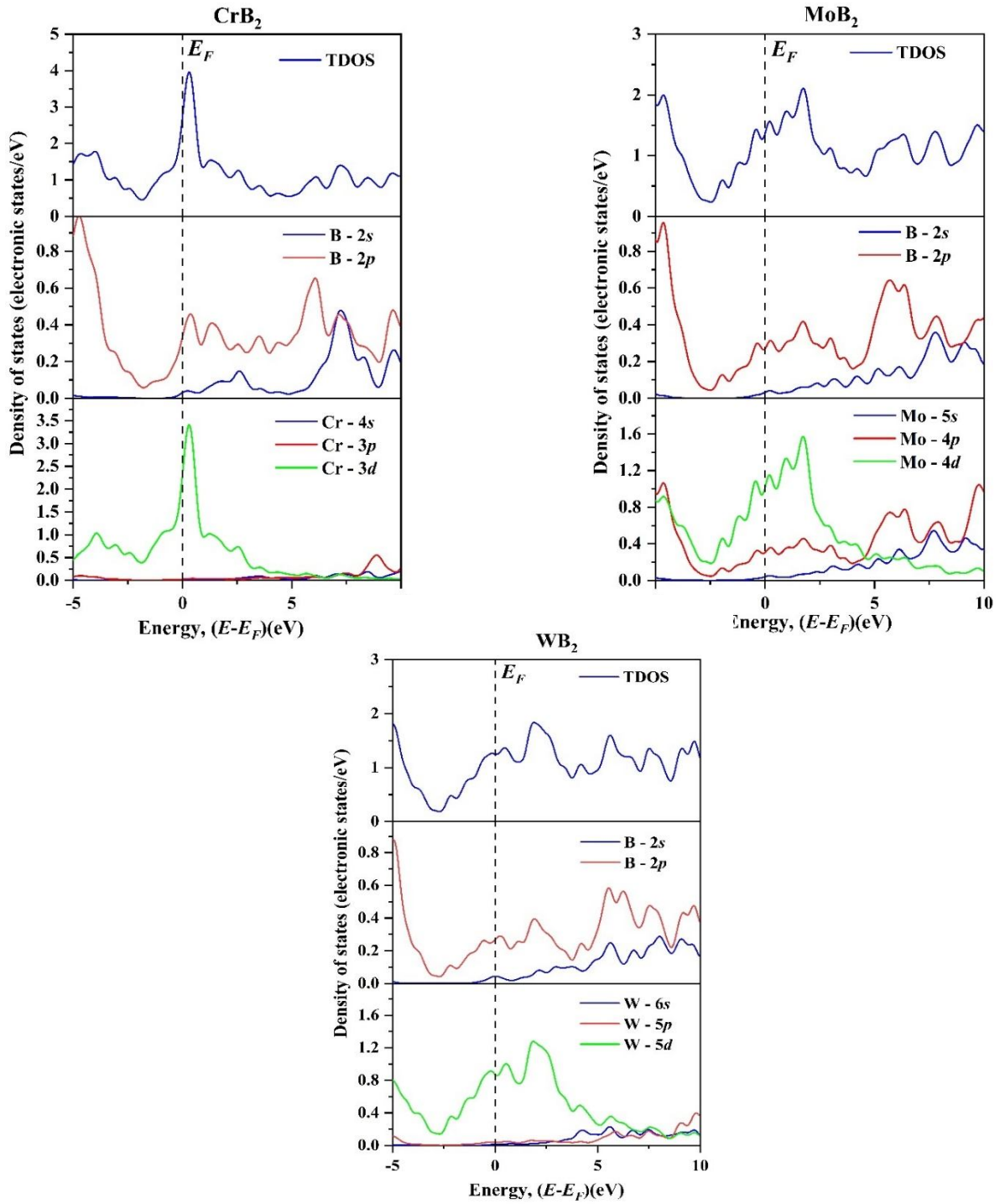


Figure 7. Total and partial electronic energy density of states of XB₂ (X = Cr, Mo and W) compounds.

3.4 Thermo-mechanical properties

(a) Acoustic behavior and its anisotropy

The relationship between sound velocity and thermal conductivity, $K = \frac{1}{3} C_v l v$ (where, C_v is the specific heat per unit volume, v is the velocity of sound in the solid, and l is the mean free path for the lattice vibrations), makes sound velocity an important parameter of a material. In this section, the longitudinal and transverse sound velocities of XB_2 ($X = \text{Cr, Mo and W}$) have been calculated. Given the bulk (B) and shear (G) moduli, the longitudinal (v_l) and the transverse (v_t) sound velocities can be computed using the following equations [91]:

$$v_t = \sqrt{\frac{G}{\rho}} \quad (37)$$

and

$$v_l = \sqrt{\frac{3B + 4G}{3\rho}} \quad (38)$$

Here, ρ is the mass-density of the solid. These formulae demonstrate that the density and elastic moduli of a material greatly affects its sound velocities. The average sound velocity, v_a , can be calculated using the longitudinal (v_l) and the transverse (v_t) sound velocities as follows [91]:

$$v_a = \left[\frac{1}{3} \left(\frac{2}{v_t^3} + \frac{1}{v_l^3} \right) \right]^{-\frac{1}{3}} \quad (39)$$

The estimated values of sound velocities of XB_2 are represented in Table 8. The average sound velocity of CrB_2 is more than that of MoB_2 and WB_2 . So, the compound, CrB_2 may behave as better room temperature heat conductor than MoB_2 and WB_2 .

The study of acoustic impedance of materials has developed over time for many underwater acoustic applications, aircraft engine design, noise reduction, transducer design, and industrial factory design. A high sound pressure will produce a high particle velocity in a medium with low impedance, but the same sound pressure will produce a relatively modest particle velocity in a medium with high impedance. The acoustic impedance of the compounds was determined using the following equation [92]:

$$Z = \sqrt{\rho G} \quad (40)$$

where G is the shear modulus and ρ is the density of the solid. The unit of acoustic impedance is the Rayl; $1 \text{ Rayl} = \text{kgm}^{-2}\text{s}^{-1} = 1 \text{ Nsm}^3$. An acoustic impedance of a material is high when its shear modulus and density are both high.

The intensity of sound radiation is another important factor in the design of sound boards and loudspeakers. The density and shear modulus of a material are related to the intensity, I , of its acoustic radiation as [92]:

$$I \approx \sqrt{G/\rho^3} \quad (41)$$

This is also known as the *radiation factor*. In sound board design, the radiation factor is usually taken into consideration while selecting materials.

Table 8: Calculated mass density ρ (kg/m^3), longitudinal velocity of sound v_l (ms^{-1}), transverse velocity of sound v_t (ms^{-1}), average sound velocity v_a (ms^{-1}), acoustic impedance Z (Rayl) and radiation factor I ($\text{m}^4/\text{kg.s}$) of XB_2 ($X = \text{Cr, Mo and W}$) compounds.

Compound	P	v_l	v_t	v_a	$Z (\times 10^6)$	I
CrB ₂	5437.49	9134.55	5273.76	5854.89	28.68	0.97
MoB ₂	7695.13	8704.82	4957.08	5509.82	38.15	0.64
WB ₂	1342.11	7273.67	3902.44	4357.78	52.39	0.29

Every atom in a solid can vibrate in one of three separate modes (one longitudinal and two transverse). In anisotropic crystals, pure longitudinal and transverse wave modes are limited only to certain crystallographic directions, whereas quasi-transverse or quasi-longitudinal modes exist in all other directions. Hexagonal symmetric crystals can exhibit pure longitudinal and transverse modes for [001] and [100] directions. The acoustic velocities of hexagonal crystals along these principal directions can be determined using the following relationships [83]:

$$[100]v_l = \sqrt{(C_{11} - C_{12})/2\rho}; [010]v_{t1} = \sqrt{C_{11}/\rho}; [001]v_{t2} = \sqrt{C_{44}/\rho} \quad (42)$$

$$[001]v_l = \sqrt{C_{33}/\rho}; [100]v_{t1} = [010]v_{t2} = \sqrt{C_{44}/\rho} \quad (43)$$

where v_{t1} and v_{t2} refers to the velocity of first transverse mode and the second transverse mode, respectively, and v_l is the velocity of the longitudinal mode. These correlations predict that a compound with high elastic constants and low density will have high sound velocities. Directional sound velocities are displayed in Table 9.

Table 9: Anisotropic sound velocities (ms^{-1}) of XB_2 ($X = \text{Cr, Mo and W}$) compounds along different crystallographic directions.

Propagation directions		Anisotropic sound velocities (ms^{-1}) for compounds		
		CrB_2	MoB_2	WB_2
[100]	$[100]v_l$	6353.8	5738.5	4144.1
	$[010]v_{t1}$	10146.5	9157.6	7309.8
	$[001]v_{t2}$	4817.1	4808.4	3880.5
[001]	$[001]v_l$	7545.3	7676.3	7058.8
	$[100]v_{t1}$	4817.1	4808.4	3880.5
	$[010]v_{t2}$	4817.1	4808.4	3880.5

Significant anisotropy in sound velocity is present in XB_2 reflecting anisotropy in the bonding strengths along different crystallographic axes.

(b) Debye temperature

The Debye temperature (θ_D) is linked to various physical properties e.g., lattice vibration, thermal conductivity, phonon-specific heat, interatomic bonding, resistivity, melting temperature, vacancy formation energy, and coefficient of thermal expansion. In conventional superconductors, it also provides the characteristic energy of the phonons that leads to Cooper pairing. It is generally observed that materials with larger Debye temperatures are those with stronger interatomic bonding strength, higher melting temperature, higher hardness, higher acoustic wave velocity, and lower average atomic mass. Moreover, Debye temperature marks the boundary between the classical and quantum behavior in lattice vibration. When $T > \theta_D$, all the modes of vibrations have almost the same energy, $\sim k_B T$. On the other hand, for $T < \theta_D$, higher frequency modes are regarded frozen, revealing the quantum mechanical nature of vibrational energy spectrum [93]. In this study, θ_D was computed as follows [91,94]:

$$\theta_D = \frac{h}{k_B} \left[\left(\frac{3n}{4\pi} \right) \frac{N_A \rho}{M} \right]^{\frac{1}{3}} v_a \quad (44)$$

where h is the Planck's constant, k_B is the Boltzmann's constant, n is the number of atoms in the unit cell, M is the molar mass, ρ is the density of the solid, N_A is the Avogadro number, and v_a denotes the average sound velocity.

As shown in Table 10, Θ_D value of CrB₂ is higher than that of MoB₂ and WB₂. The estimated values of Θ_D of XB₂ (X = Cr, Mo and W) compounds exhibit excellent agreement with the earlier findings.

(c) Melting temperature

Melting point is a key thermo-physical factor useful for verifying the feasibility of using solids at high temperatures. A high melting temperature indicates strong atomic bonding, a high heat of fusion, low entropy of fusion, or a combination of both, as well as a low thermal expansion value [96]. We have calculated the melting point (T_m) of hexagonal crystals using the elastic stiffness constants from an empirical formula proposed by Fine et al. [95]:

$$T_m = 354 K + 4.5(K/GPa) \left(\frac{2C_{11} + C_{33}}{3} \right) \quad (45)$$

The calculated melting temperatures are enlisted in Table 10. All three XB₂ (X = Cr, Mo and W) compounds possess high melting point. Generally speaking, a solid has a greater melting temperature when its Young's modulus is higher, and vice versa [96,97]. Because of higher elastic constants (C_{11} and C_{33}) and Young's modulus of WB₂, the melting point of WB₂ is higher than that of MoB₂ and CrB₂, which means WB₂ is a better candidate material for high temperature application compared to MoB₂ and CrB₂.

(d) Thermal expansion coefficient and heat capacity

The thermal expansion coefficient (α) (TEC) is another important thermomechanical parameter controlled by the bonding strength and lattice anharmonicity. This particular parameter is linked to a variety of other physical properties, including specific thermal conductivity, heat, temperature variation of the energy band gap in semiconductors, and effective mass of electron/hole. The thermal expansion coefficient of a solid can be calculated using the following equation [93]:

$$\alpha = \frac{1.6 \times 10^{-3}}{G} \quad (46)$$

The thermal expansion coefficient is inversely related to the melting temperature: $\alpha \approx 0.02T_m$ [92,98]. The computed TECs are disclosed in Table 10.

The heat capacity per unit volume (ρC_P) is the change in thermal energy per unit volume of a substance per degree Kelvin change in temperature. Materials with higher heat capacity exhibit lower thermal diffusivity and higher thermal conductivity. These materials have a high capacity for heat storage. We have calculated ρC_P for XB₂ (X = Cr, Mo and W) compounds using the following equation [92]:

$$\rho C_P = \frac{3k_B}{\Omega} \quad (47)$$

where, $(1/\Omega)$ is the number of atoms per unit volume. Table 10 shows the heat capacity per unit volume of metallic diborides. The heat capacity of CrB₂ is higher than those of MoB₂ and WB₂. It follows that CrB₂ should have a relatively higher thermal conductivity.

Table 10: Number of atoms per unit volume n (atoms/m³), elastic Debye temperature Θ_D (K), melting temperature T_m (K), thermal expansion coefficient α (K⁻¹), and heat capacity per unit volume ρC_p (JK⁻¹m⁻³) of XB₂ (X = Cr, Mo and W) compounds.

Compound	n (10 ²⁸)	Θ_D	T_m	α (10 ⁻⁵)	ρC_p (10 ⁶)	Reference
CrB ₂	13.34	890.84	2498.13	1.06	5.52	This work
	-	941.00	-	-	-	[17]
MoB ₂	11.82	805.91	2970.15	0.85	4.89	This work
	-	783.00	-	-	-	[17]
WB ₂	11.80	636.44	3509.15	0.78	4.88	This work
	-	624.20	-	-	-	[22]

(e) Lattice thermal conductivity

The ability of a material to transport heat through lattice vibrations is measured by its lattice thermal conductivity (k_{ph}) at various temperatures. The lattice thermal conductivity plays a crucial role in many technological applications as a design parameter. For example, low thermal conductivity is preferred for thermoelectric (TE) conversions and for thermal barrier coating (TBC) materials. On the other hand, high lattice thermal conductivity materials find extensive application in heat sinks [99]. Slack developed an empirical formula to theoretically estimate the k_{ph} [100]:

$$k_{ph} = A(\mathcal{G}) \frac{M_{av} \Theta_D^3 \delta}{\gamma^2 n^{2/3} T} \quad (48)$$

In the above equation, M_{av} is the average atomic mass in kg/mol, δ is the cubic root of average atomic volume in meter (m), Θ_D is the Debye temperature in K, T is the absolute temperature in K, n is the number of atoms in the conventional unit cell, and γ is the acoustic Grüneisen parameter that measures the degree of anharmonicity of the phonons. A material with a low Grüneisen parameter has low phonon anharmonicity, resulting in high thermal conductivity. The dimensionless quantity $A(\gamma)$ may be computed from the Poisson's ratio [100]:

$$\gamma = \frac{3(1 + \nu)}{2(2 - 3\nu)} \quad (49)$$

The factor $A(\gamma)$, due to Julian [101], is calculated from:

$$A(\gamma) = \frac{5.720 \times 10^7 \times 0.849}{2 \times (1 - 0.514/\gamma + 0.228/\gamma^2)} \quad (50)$$

The estimated lattice thermal conductivity at room temperature (300 K) and the Grüneisen parameter are given in Table 11. It is found that the compound MoB₂ shows higher k_{ph} than that of CrB₂ and WB₂.

(f) Minimum thermal conductivity and its anisotropy

The phonon thermal conductivity of a substance reaches its lower limit at higher temperature, which is known as the minimum thermal conductivity of that material. In this case, the interatomic distance is taken to be the mean free path of the phonons. The following formula for determining the minimum thermal conductivity, k_{min} , of materials at high temperatures was developed by Clarke [98] using the quasi-harmonic Debye model:

:

$$k_{min} = k_B \nu_a (V_{atomic})^{-2/3} \quad (51)$$

where, k_B is the Boltzmann constant, ν_a is the average sound velocity and V_{atomic} represents the cell volume per atom of the compound.

The calculated values of minimum thermal conductivity of the XB₂ (X = Cr, Mo and W) compounds are also tabulated in Table 11. The k_{min} of CrB₂ is higher than that of MoB₂ and WB₂. Higher minimum thermal conductivity is seen in compounds with higher sound velocity and Θ_D .

An elastically anisotropic material has anisotropic minimum thermal conductivity. Anisotropic thermal conductivity materials gain extensive application in thermal barrier coatings, thermoelectrics, heat shields, and heat spreading in electronic and optical device technologies. Anisotropy in minimum thermal conductivity is influenced by the different sound velocities corresponding to different crystallographic directions. The following minimum thermal conductivities are calculated along various directions using the Cahill model [102]:

$$k_{min} = \frac{k_B}{2.48} n^{2/3} (\nu_l + \nu_{t1} + \nu_{t2}) \quad (52)$$

where, $n = N/V$ = number of atoms per unit volume. The minimum thermal conductivities of XB₂ (X = Cr, Mo and W) compounds along the [100] and [001] directions are shown in Table

11. The minimum thermal conductivities along different crystallographic axes of XB_2 compounds appear to be higher than the isotropic minimum thermal conductivity.

Table 11: Grüneisen parameter γ , lattice thermal conductivity k_{ph} (W/m-K), minimum thermal conductivities k_{\min} in different crystallographic directions (all in W/m-K), and minimum thermal conductivity k_{\min} in Cahill's and Clark's method (both in W/m-K) of XB_2 ($X = \text{Cr}, \text{Mo}$ and W) compounds.

Compound	γ	k_{ph}	[100] k_{\min}	[001] k_{\min}	k_{\min}	
					Cahill	Clark
CrB_2	1.50	77.39	3.10	2.50	2.80	2.11
MoB_2	1.55	90.60	2.64	2.32	2.48	1.83
WB_2	1.76	57.87	2.05	1.98	2.02	1.45

3.5 Optical parameters

Optical parameters such as absorption coefficient $\alpha(\omega)$, optical conductivity $\sigma(\omega)$, dielectric function $\epsilon(\omega)$, loss function $L(\omega)$, reflectivity $R(\omega)$, and refractive index $N(\omega)$ [where $\omega = 2\pi f$ is the angular frequency of the incident electromagnetic wave (EMW)] are crucial for analyzing optical response of a material to incident light [103–105]. All the optical parameters are intimately related to the electronic band structure. In this section, we have provided the findings of the computed optical properties of XB_2 ($X = \text{Cr}, \text{Mo},$ and W) compounds for incident EMW energies up to 30 eV with electric field polarizations along the [100] and [001] directions, as depicted in Figures (8-10). Since the binary metallic diborides XB_2 have hexagonal symmetry, the directions [100] and [001] of incident photon refers to directions of related electric field at right angles and parallel to crystallographic c-axis, respectively.

The absorption coefficient, $\alpha(\omega)$, tells us how much light with a certain energy may enter a material before being absorbed and aids in determining a substance's ideal solar energy conversion efficiency. Low absorption coefficient materials merely absorb light weakly; if they are thin enough, they will turn transparent at certain wavelengths. It also indicates the electrical properties of a material, such as whether it is insulating, metallic, or semiconducting. The variation of the absorption coefficient $\alpha(\omega)$ as a function of photon energy is shown in Figures 8(a), 9(a), and 10(a). The absorption coefficient of all three metallic diborides begins from 0 eV of photon energy, confirming that they have metallic electronic band structures. XB_2 compounds have high absorption coefficient in the ultraviolet (UV) region, ranging from 3.5 to 25.0 eV in the spectral region. CrB_2 and MoB_2 have larger peak values for [100] polarization than for [001]

polarization, whereas WB_2 has higher peak values for [001] polarization than for [100] polarization, demonstrating optical anisotropy in absorption properties.

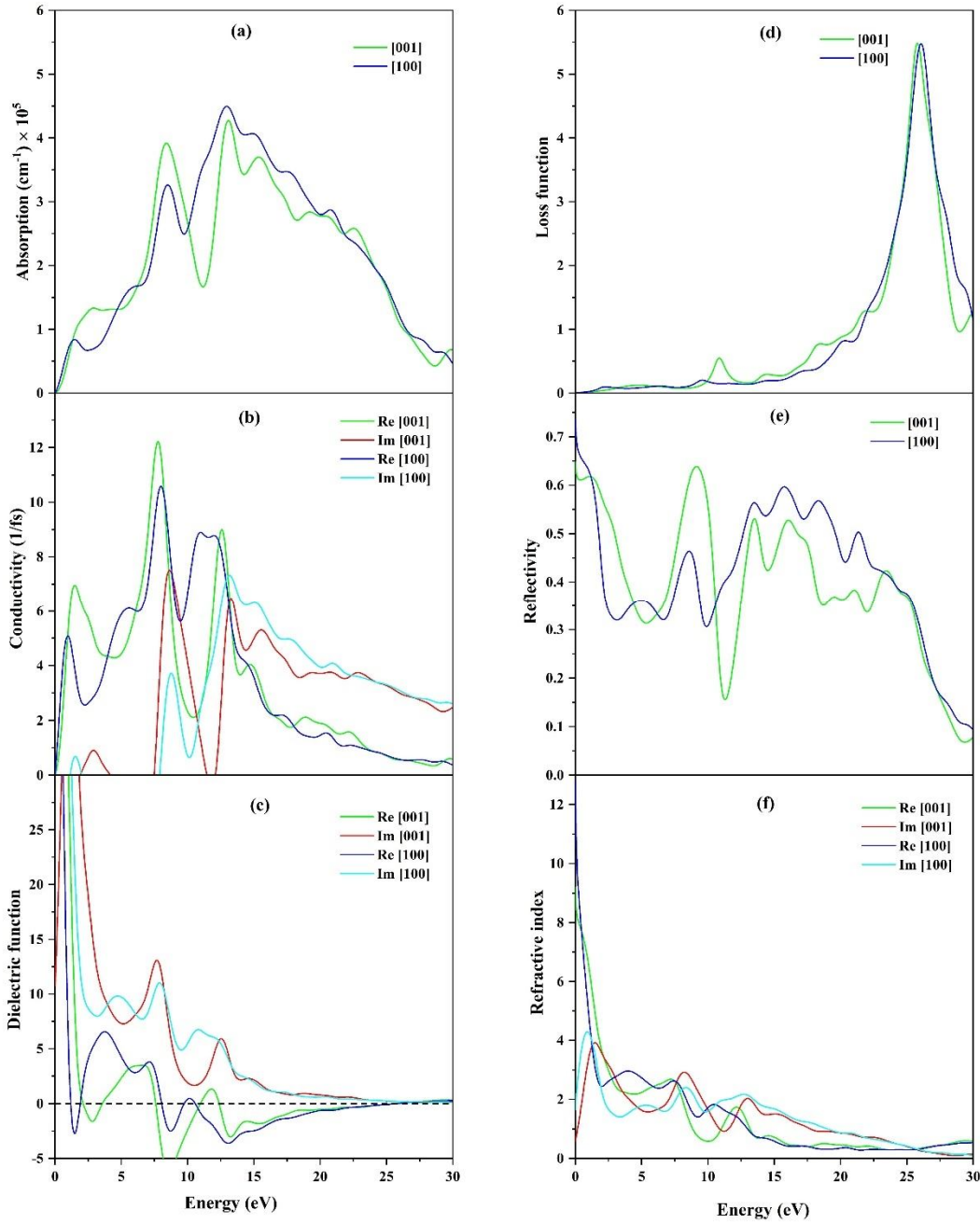


Figure 8. The energy dependent (a) absorption coefficient (b) optical conductivity (c) dielectric function (d) loss function (e) reflectivity, and (f) refractive index of CrB_2 with electric polarization vectors along the [100] and [001] directions.

Another crucial optoelectronic property of a material is its optical conductivity, $\sigma(\omega)$, which is the conduction of free charge carriers within a certain range of photon energy. An accurate predictor of photoconductivity is optical conductivity [106].

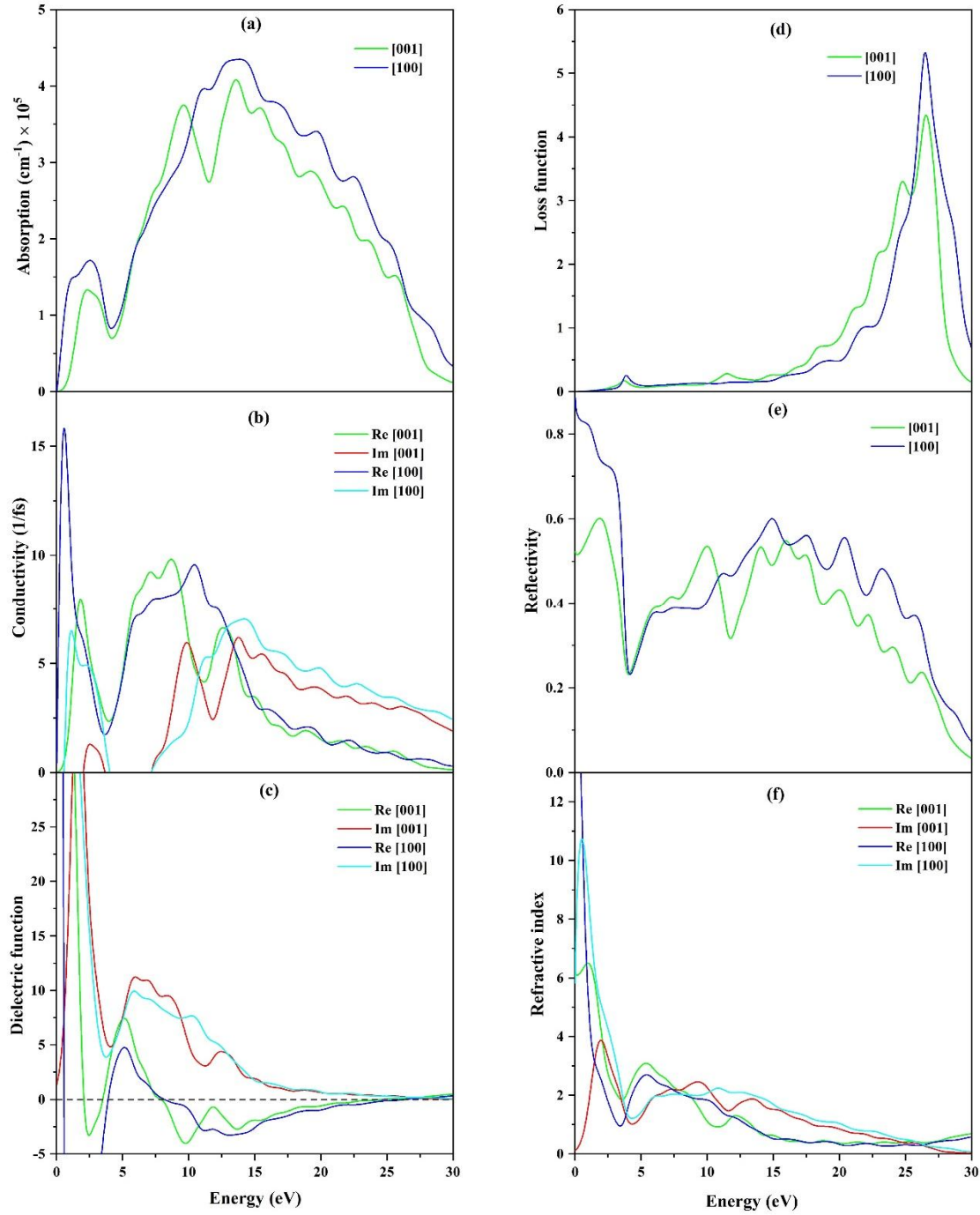


Figure 9. The energy dependent (a) absorption coefficient (b) optical conductivity (c) dielectric function (d) loss function (e) reflectivity, and (f) refractive index of MoB₂ with electric polarization vectors along the [100] and [001] directions.

Photoconductivity starts with zero photon energy in both polarization directions [Figures 8(b), 9(b), and 10(b)], which is a hallmark of metallic conductivity of XB₂ and is perfectly consistent with its electronic band structure and TDOS predictions. In the photon energy range of 0 to 15

eV for the compounds, the spectra for both polarizations show significant variation, indicating that their optical properties are anisotropic. In the mid-UV range, the optical conductivity falls with increasing energy.

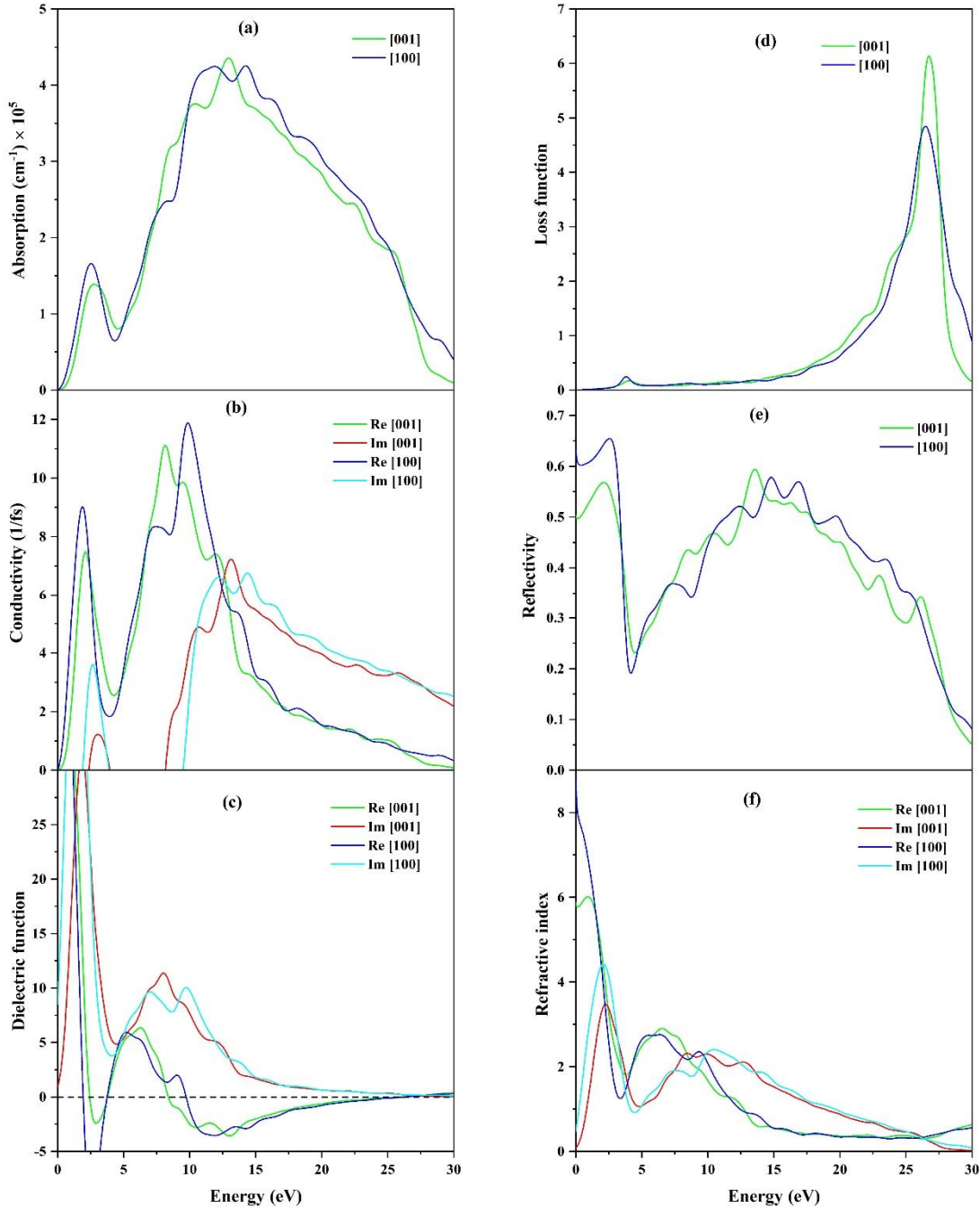


Figure 10. The energy dependent (a) absorption coefficient (b) optical conductivity (c) dielectric function (d) loss function (e) reflectivity, and (f) refractive index of WB_2 with electric polarization vectors along the [100] and [001] directions.

Figures 8(c), 9(c), and 10(c) display the real and imaginary parts of the dielectric constants. The real part $\varepsilon_1(\omega)$ is connected to the electrical polarization of the material, while the imaginary part $\varepsilon_2(\omega)$ is connected to the dielectric loss. The non-zero value of $\varepsilon_1(0)$ indicates the high availability of free charge carriers in these metallic systems. For the three compounds, there is a noticeable anisotropy in both spectra as a result of the differing polarizations. For all three compounds, the real part of the dielectric function crosses zero from below at ~ 26.50 eV, while the imaginary part flattens to a very low value at the same energy. This indicates that the material becomes transparent to the incident EMW above 26.50 eV. This phenomenon validates the Drude-like behavior (metallic feature) of XB_2 . The frequency at which $\varepsilon_1(\omega)$ evolves from negative to positive values along with $\varepsilon_2(\omega) < 1$ is known as the plasma frequency, ω_p . At this frequency, the free electrons in a system are collectively excited. For high frequency or power applications, low values of $\varepsilon_2(\omega)$ are favored in order to minimize electric power loss. Conversely, for small-sized capacitance applications, high values of $\varepsilon_1(\omega)$ are advised.

The loss function, $L(\omega)$, is an essential optical parameter describing the energy loss of a fast electron moving in a material. In this instance, the energy of the rapidly moving charge is attenuated, leading to a collective electronic excitation that is referred to as a plasma excitation. It is noteworthy that the plasma energies correspond with a rapid decrease in absorption coefficient and reflectance. As a result, it is anticipated that the compound under investigation would exhibit transparent behavior for photon energies higher than the plasma energy, and its optical characteristics will resemble those of insulating systems. Figures 8(d), 9(d), and 10(d) show that for [100] and [001] polarization directions, the peaks of $L(\omega)$ are located at ~ 26.50 eV. Above the plasma energy, optical behavior of a metal shifts to dielectric-like response. MoB_2 exhibits a higher peak value for [100] polarization direction than [001] polarization direction, WB_2 exhibits a higher peak value for [001] polarization direction than [100] polarization direction, and CrB_2 exhibits a slightly higher peak value for [001] polarization direction, indicating optical anisotropy in the loss function.

Reflectivity, $R(\omega)$, measures the fraction of the incident light energy reflected from the material. The compounds XB_2 ($X = \text{Cr}, \text{Mo}, \text{and W}$) exhibit excellent infrared and visible light reflectivity, as seen by Figures 8(e), 9(e), and 10(e). The highest reflectivity values in the infrared light region due to polarization [100] is 68.70% for CrB_2 , 85.60% for MoB_2 , 61.60% for WB_2 while for polarization [001] the corresponding values are 61.90%, 52.40%, and 49.50%, respectively. For both polarizations, the average reflectivity of XB_2 within visible light region is above 44%, which is enough for them to be a potential coating material to diminish solar heat [38,103]. It is observed that the maximum average reflectivity is found for MoB_2 .

The energy dependent refractive index, $N(\omega)$, is an optical parameter important for photonic device fabrication, such as for constructing optical wave-guides. In fact, $N(\omega) = n(\omega) + ik(\omega)$, where $k(\omega)$ is the extinction coefficient. The refractive index $n(\omega)$ (real part of complex index of refraction) of a material is a number that refers to how fast light travels through the material.

The amount of light that is reflected at the contact is likewise determined by the refractive index. Throughout the visible spectrum, the refractive index of the majority of materials changes by a few percent with photon energy. The $n(\omega)$ spectra (Figures 8(f), 9(f), and 10(f)) for all the three compounds exhibit anisotropic nature. Compared to CrB₂ and WB₂, the average real part of refractive index of MoB₂ has a very high value at low energies encompassing the infrared regions. Systems with a high refractive index provide advantageous optical characteristics for optical display devices and photonic crystals.

The imaginary component of the complex index of refraction, known as the extinction coefficient, regulates how quickly light is occluded. In addition, it quantifies the strength of a material's absorption of light at a certain wavelength per mass density or per molar concentration and characterizes the decrease of electromagnetic radiation in a medium. The extinction coefficient is associated with the conductive properties of materials. The extinction coefficient of metallic materials is significant, whereas that of semiconducting materials is minimal. In contrast, dielectric materials are essentially non-conductors whose extinction coefficient is zero. A large static value of $k(\omega)$ of MoB₂ indicates that the metallic conductivity of MoB₂ is greater than that of CrB₂ and WB₂. In the high energy region where $n(\omega)$ begins to increase and achieves an almost constant value for all compounds, $k(\omega)$ becomes zero.

3.6 Superconducting state properties

XB₂ (X = Cr, Mo and W) compounds exhibit phonon mediated superconductivity. For conventional superconductors where electron-phonon interactions lead to Cooper pairing, the superconducting transition temperature can be expressed as [38,85,107,108]:

$$T_c = \frac{\theta_D}{1.45} \exp \left[-\frac{1.04(1 + \lambda_{ep})}{\lambda_{ep} - \mu^*(1 + 0.62\lambda_{ep})} \right] \quad (53)$$

where μ^* is the Coulomb pseudopotential and λ_{ep} is the electron-phonon coupling constant.

The electron-electron interaction parameter of a material, termed as the repulsive Coulomb pseudopotential, can be calculated as follows from the electronic density of states at the Fermi energy [110]:

$$\mu^* = \frac{0.26 N(E_F)}{1 + N(E_F)} \quad (54)$$

where, $N(E_F)$ is the total density of states at the Fermi level of the compound. The repulsive Coulomb pseudopotential is responsible to lower the transition temperature, T_c , of superconducting compounds [109,110]. It also gauges how strongly electrons are correlated inside a system. The electron-phonon coupling constant can be estimated approximately using the equation presented below [111,112]:

$$\lambda_{ep} = \frac{\gamma_{cal}}{\gamma_{free}} - 1 \quad (55)$$

where γ_{cal} is the theoretical electronic specific heat capacity constant calculated from the DOS at Fermi level and γ_{free} is the theoretical electronic specific heat capacity constant estimated from the free electron gas model. In this work, we have calculated γ_{cal} and γ_{free} of XB_2 materials by using the following equations [112-114]:

$$\gamma_{cal} = \frac{\pi^2 k_B^2 N(E_F)}{3}$$

$$\gamma_{free} = \frac{\pi^2 n_e k_B^2}{2E_F}$$

where, n_e denotes the free electron number density and E_F is the Fermi energy. The resulting γ_{cal} value obtained using the $N(E_F)$ from the band structure calculations differs from the γ_{free} of XB_2 . This is expected since the DOS value obtained from the free electron model is not *dressed* properly by the electron-ion interaction.

Table 12 displays the determined superconducting parameters, including the critical temperatures of XB_2 compounds. The T_c values obtained show reasonable agreement with the experimental ones.

Table 12. Parameters related to superconductivity of XB_2 (X = Cr, Mo and W) compounds.

Compound	$N(E_F)$ (States per eV)	μ^*	γ (mJ/mol-K ²)	λ_{ep}	T_c (K)	Reference
CrB ₂	2.52	0.19	5.94	0.67	8.09	This work
	-	-	-		7.00	[21]
MoB ₂	1.34	0.15	3.16	0.88	27.12	This work
	-	0.13	-	1.67	32.00	[19]
WB ₂	1.25	0.14	2.95	0.57	6.02	This work
	-	-	-	-	5.40	[115]

4. Conclusions

To summarize, we have presented a comprehensive study of the structural, mechanical, electronic, optical, superconducting state and thermophysical properties of binary metal diborides XB_2 (X = Cr, Mo and W) using a first-principles calculations based on density functional theory. Our calculated equilibrium structural parameters and elastic constants of XB_2 are consistent with the previously published data [11-13,15,22].

XB_2 ($X = \text{Cr, Mo and W}$) compounds have high machinability, high hardness values, and an exceptionally high melting temperature, making them ideal for use as heavy-duty engineering tools that can withstand highly hostile and abrasive environments. Importantly, WB_2 is mechanically superior to MoB_2 and CrB_2 , because its Young's modulus, shear modulus and hardness are higher than those of MoB_2 and CrB_2 . WB_2 is also ductile in nature, whereas MoB_2 and CrB_2 are brittle. Ductility together with very high hardness makes WB_2 a very useful compound for structural engineering. The band structure and total density of states investigations indicate that XB_2 ($X = \text{Cr, Mo and W}$) compounds are metallic with considerable TDOS at the Fermi level. For all of the XB_2 ($X = \text{Cr, Mo, and W}$) compounds, the computed Debye temperatures are high, suggesting their hard nature. High melting points and lattice thermal conductivity values match extremely well to estimated hardness and elastic moduli. The optical parameters exhibit metallic behavior consistent with the electronic band structure. The anisotropy levels in elastic and optical properties of WB_2 are less than those of MoB_2 and CrB_2 . All of the compounds investigated here be utilized as a coating to minimize solar heating, with MoB_2 being the most promising contender. All the compounds under study are effective UV radiation absorbers. We have explored the superconducting state properties of XB_2 ($X = \text{Cr, Mo and W}$) and found that the compound MoB_2 shows the highest superconducting transition temperature. The high- T_c results from a high electron-phonon coupling constant for MoB_2 compared to the other two metallic diborides.

Declaration of interest

The authors declare that they have no known competing financial interests or personal relationships that could have appeared to influence the work reported in this paper.

Data availability

The data sets generated and/or analyzed in this study are available from the corresponding author on reasonable request.

CRedit author statement

Razu Ahmed: Methodology, Software, Formal analysis, Writing- Original draft. **Md. Sohel Rana:** Methodology, Software, Formal analysis. **Md. Sajidul Islam:** Software, Validation. **S.H. Naqib:** Conceptualization, Supervision, Formal analysis, Writing- Reviewing and Editing.

References

[1]	R. B. Kaner, J. J. Gilman, and S. H. Tolbert, <i>Designing Superhard Materials</i> , Science 308 , 1268 (2005).
[2]	P. F. McMillan, <i>New Materials from High-Pressure Experiments</i> , Nat. Mater. 1 , 19 (2002).

[3]	P. Wang, R. Kumar, E. M. Sankaran, X. Qi, X. Zhang, D. Popov, A. L. Cornelius, B. Li, Y. Zhao, and L. Wang, <i>Vanadium Diboride (VB₂) Synthesized at High Pressure: Elastic, Mechanical, Electronic, and Magnetic Properties and Thermal Stability</i> , <i>Inorg. Chem.</i> 57 , 1096 (2018).
[4]	R. Mohammadi, A. T. Lech, M. Xie, B. E. Weaver, M. T. Yeung, S. H. Tolbert, and R. B. Kaner, <i>Tungsten Tetraboride, an Inexpensive Superhard Material</i> , <i>Proc. Natl. Acad. Sci. U.S.A.</i> 108 , 10958 (2011).
[5]	S. Carencio, D. Portehault, C. Boissière, N. Mézailles, and C. Sanchez, <i>Nanoscaled Metal Borides and Phosphides: Recent Developments and Perspectives</i> , <i>Chem. Rev.</i> 113 , 7981 (2013).
[6]	D. Yu Wang, X. Li, and Y. Xu Wang, <i>First-Principles Investigation of Hexagonal WB₂ Surfaces</i> , <i>J. Phys. Soc. Jpn.</i> 81 , 044712 (2012).
[7]	R. W. G. Wyckoff, <i>Crystal Structures-Volume 1</i> (Wiley, New York, 1965).
[8]	P. Beck, <i>Metallurgy: Electronic Structure and Alloy Chemistry of the Transition Elements</i> (Interscience-Wiley, New York, 1963).
[9]	AmreenBano and N. K. Gaur, <i>Chemical Topology of 2-Dimensional MoB₂ Sheet: First-Principles Study</i> , <i>AIP Conf. Proc.</i> 2265 , 030686 (2020).
[10]	H.-Y. Chung, M. B. Weinberger, J. B. Levine, A. Kavner, J.-M. Yang, S. H. Tolbert, and R. B. Kaner, <i>Synthesis of Ultra-Incompressible Superhard Rhenium Diboride at Ambient Pressure</i> , <i>Science</i> 316 , 436 (2007).
[11]	S. Wang et al., <i>Crystal Structures, Elastic Properties, and Hardness of High-Pressure Synthesized CrB₂ and CrB₄</i> , <i>J. Superhard Mater.</i> 36 , 279 (2014).
[12]	Q. Tao, X. Zhao, Y. Chen, J. Li, Q. Li, Y. Ma, J. Li, T. Cui, P. Zhu, and X. Wang, <i>Enhanced Vickers Hardness by Quasi-3D Boron Network in MoB₂</i> , <i>RSC Adv.</i> 3 , 18317 (2013).
[13]	H. P. Woods, F. E. Wawner, and B. G. Fox, <i>Tungsten Diboride: Preparation and Structure</i> , <i>Science</i> 151 , 75 (1966).
[14]	M. Eisterer, J. Emhofer, S. Sorta, M. Zehetmayer, and H. W. Weber, <i>Connectivity and Critical Currents in Polycrystalline MgB₂</i> , <i>Supercond. Sci. Technol.</i> 22 , 034016 (2009).
[15]	I. R. Shein and A. L. Ivanovskii, <i>Elastic Properties of Mono- and Polycrystalline Hexagonal AlB₂ -like Diborides of s, p and d Metals from First-Principles</i>

	<i>Calculations</i> , J. Phys.: Condens. Matter 20 , 415218 (2008).
[16]	A. Bauer, A. Regnat, C. G. F. Blum, S. Gottlieb-Schönmeyer, B. Pedersen, M. Meven, S. Wurmehl, J. Kuneš, and C. Pfleiderer, <i>Low-Temperature Properties of Single-Crystal CrB₂</i> , Phys. Rev. B 90 , 064414 (2014).
[17]	V. Dovale-Farelo, P. Tavadze, M. J. Verstraete, A. Bautista-Hernández, and A. H. Romero, <i>Exploring the Elastic and Electronic Properties of Chromium Molybdenum Diboride Alloys</i> , J. Alloys. Compd. 866 , 158885 (2021).
[18]	G. Akopov, M. T. Yeung, and R. B. Kaner, <i>Rediscovering the Crystal Chemistry of Borides</i> , Adv. Mater. 29 , 1604506 (2017).
[19]	Y. Quan, K.-W. Lee, and W. E. Pickett, <i>MoB₂ under Pressure: Superconducting Mo Enhanced by Boron</i> , Phys. Rev. B 104 , 224504 (2021).
[20]	C. Pei et al., <i>Pressure-Induced Superconductivity at 32 K in MoB₂</i> , Natl. Sci. Rev. 10 , nwad034 (2023).
[21]	C. Pei et al., <i>Pressure-Induced Superconductivity in Itinerant Antiferromagnet CrB₂</i> , arXiv:2109.15213.
[22]	X. Hao, Y. Xu, Z. Wu, D. Zhou, X. Liu, X. Cao, and J. Meng, <i>Low-Compressibility and Hard Materials ReB₂ and WB₂: Prediction from First-Principles Study</i> , Phys. Rev. B 74 , 224112 (2006).
[23]	N. L. Okamoto, M. Kusakari, K. Tanaka, H. Inui, and S. Otani, <i>Anisotropic Elastic Constants and Thermal Expansivities in Monocrystal CrB₂, TiB₂, and ZrB₂</i> , Acta Mater. 58 , 76 (2010).
[24]	W. Kohn and L. J. Sham, <i>Self-Consistent Equations Including Exchange and Correlation Effects</i> , Phys. Rev. 140 , A1133 (1965).
[25]	S. J. Clark, M. D. Segall, C. J. Pickard, P. J. Hasnip, M. I. J. Probert, K. Refson, and M. C. Payne, <i>First Principles Methods Using CASTEP</i> , Z. Kristallogr. 220 , 567 (2005).
[26]	J. P. Perdew, K. Burke, and M. Ernzerhof, <i>Generalized Gradient Approximation Made Simple</i> , Phys. Rev. Lett. 77 , 3865 (1996).
[27]	M. Lewin, E. H. Lieb, and R. Seiringer, <i>The Local Density Approximation in Density Functional Theory</i> , Pure Appl. Analysis 2 , 35 (2020).
[28]	V. Sahni, K.-P. Bohnen, and M. K. Harbola, <i>Analysis of the Local-Density</i>

	<i>Approximation of Density-Functional Theory</i> , Phys. Rev. A 37 , 1895 (1988).
[29]	D. Vanderbilt, <i>Soft Self-Consistent Pseudopotentials in a Generalized Eigenvalue Formalism</i> , Phys. Rev. B 41 , 7892 (1990).
[30]	M. C. Payne, M. P. Teter, D. C. Allan, T. A. Arias, and J. D. Joannopoulos, <i>Iterative Minimization Techniques for Ab Initio Total-Energy Calculations: Molecular Dynamics and Conjugate Gradients</i> , Rev. Mod. Phys. 64 , 1045 (1992).
[31]	T. H. Fischer and J. Almlof, <i>General Methods for Geometry and Wave Function Optimization</i> , J. Phys. Chem. 96 , 9768 (1992).
[32]	O. H. Nielsen and R. M. Martin, <i>First-Principles Calculation of Stress</i> , Phys. Rev. Lett. 50 , 697 (1983).
[33]	J. P. Watt, <i>Hashin-Shtrikman Bounds on the Effective Elastic Moduli of Polycrystals with Orthorhombic Symmetry</i> , J. Appl. Phys. 50 , 6290 (1979).
[34]	J. P. Watt and L. Peselnick, <i>Clarification of the Hashin-Shtrikman Bounds on the Effective Elastic Moduli of Polycrystals with Hexagonal, Trigonal, and Tetragonal Symmetries</i> , J. Appl. Phys. 51 , 1525 (1980).
[35]	S. Saha, T. P. Sinha, and A. Mookerjee, <i>Electronic Structure, Chemical Bonding, and Optical Properties of Paraelectric</i> , Phys. Rev. B 62 , 8828 (2000).
[36]	G. Murtaza, N. Yousaf, M. Yaseen, A. Laref, and S. Azam, <i>Systematic Studies of the Structural and Optoelectronic Characteristics of CaZn_2X_2 ($X = \text{N, P, As, Sb, Bi}$)</i> , Mater. Res. Express 5 , 016304 (2018).
[37]	R. Ahmed, M. Mahamudujjaman, M. A. Afzal, M. S. Islam, R. S. Islam, and S. H. Naqib, <i>DFT Based Comparative Analysis of the Physical Properties of Some Binary Transition Metal Carbides XC ($X = \text{Nb, Ta, Ti}$)</i> , J. Mater. Res. Technol. 24 , 4808 (2023).
[38]	R. Ahmed, M. Islam, M. M. Hossain, M. A. Ali, M. M. Uddin, and S. H. Naqib, <i>A Comprehensive First-Principles Insights into the Physical Properties of Binary Intermetallic Zr_3Ir Compound</i> , Results Mater. 21 , 100518 (2024).
[39]	Md. S. Islam, R. Ahmed, Md. Mahamudujjaman, R. S. Islam, and S. H. Naqib, <i>A Comparative Study of the Structural, Elastic, Thermophysical, and Optoelectronic Properties of CaZn_2X_2 ($X = \text{N, P, As}$) Semiconductors via Ab-Initio Approach</i> , Results Phys. 44 , 106214 (2023).
[40]	B. Aronsson, T. Lundström, and S. Rundqvist, <i>Borides, Silicides, and Phosphides: A</i>

	<i>Critical Review of Their Preparation, Properties and Crystal Chemistry</i> (Methuen, 1965).
[41]	W. E. Pearson, <i>The Crystal Chemistry and Physics of Metals and Alloys</i> (New York: Interscience, 1972)
[42]	M. I. Naher, M. Mahamudujjaman, A. Tasnim, R. S. Islam, and S. H. Naqib, <i>Ab-Initio Insights into the Elastic, Bonding, Phonon, Optoelectronic and Thermophysical Properties of SnTaS₂</i> , <i>Solid State Sci.</i> 131 , 106947 (2022).
[43]	M. A. Hadi, M. Zahangir Alam, I. Ahmed, A. M. M. Tanveer Karim, S. H. Naqib, A. Chroneos, and A. K. M. A. Islam, <i>A Density Functional Theory Approach to the Effects of C and N Substitution at the B-Site of the First Boride MAX Phase Nb₂SB</i> , <i>Mater. Today Commun.</i> 29 , 102910 (2021).
[44]	W. Voigt, <i>Lehrbuch der Kristallphysik (mit Ausschluss der Kristalloptik)</i> , (Vieweg + Teubner Verlag, 1966).
[45]	A. Reuss, <i>Berechnung Der Fließgrenze von Mischkristallen Auf Grund Der Plastizitätsbedingung Für Einkristalle</i> , <i>Z. Angew. Math. Mech.</i> 9 , 49 (1929).
[46]	R. Hill, <i>The Elastic Behaviour of a Crystalline Aggregate</i> , <i>Proc. Phys. Soc. A</i> 65 , 349 (1952).
[47]	R. Hill, <i>Elastic Properties of Reinforced Solids: Some Theoretical Principles</i> , <i>J. Mech. Phys. Solids</i> 11 , 357 (1963).
[48]	M. Mattesini, R. Ahuja, and B. Johansson, <i>Cubic Hf₃N₄ and Zr₃N₄: A Class of Hard Materials</i> , <i>Phys. Rev. B</i> 68 , 184108 (2003).
[49]	L. Kleinman, <i>Deformation Potentials in Silicon. I. Uniaxial Strain</i> , <i>Phys. Rev.</i> 128 , 2614 (1962).
[50]	M. Jamal, S. Jalali Asadabadi, I. Ahmad, and H. A. Rahnamaye Aliabad, <i>Elastic Constants of Cubic Crystals</i> , <i>Comput. Mat. Sci.</i> 95 , 592 (2014).
[51]	W. Feng and S. Cui, <i>Mechanical and Electronic Properties of Ti₂AlN and Ti₄AlN₃: A First-Principles Study</i> , <i>Can. J. Phys.</i> 92 , 1652 (2014).
[52]	Z. Sun, D. Music, R. Ahuja, and J. M. Schneider, <i>Theoretical Investigation of the Bonding and Elastic Properties of Nanolayered Ternary Nitrides</i> , <i>Phys. Rev. B</i> 71 , 193402 (2005).
[53]	M. E. Eberhart and T. E. Jones, <i>Cauchy Pressure and the Generalized Bonding Model</i>

	<i>for Nonmagnetic Bcc Transition Metals</i> , Phys. Rev. B 86 , 134106 (2012).
[54]	Y. Wu, Y. Duan, X. Wang, M. Peng, L. Shen, and H. Qi, <i>Elastic Anisotropy and Thermal Properties of Zr-Al-N Ternary Nitrides Using First-Principles Explorations</i> , Mater. Today Commun. 33 , 104651 (2022).
[55]	C. Kittel, <i>Introduction to Solid State Physics</i> , 8th ed. (John Wiley & Sons, Hoboken, NJ, 2005).
[56]	A. Yildirim, H. Koc, and E. Deligoz, <i>First-Principles Study of the Structural, Elastic, Electronic, Optical, and Vibrational Properties of Intermetallic Pd₂Ga</i> , Chinese Phys. B 21 , 037101 (2012).
[57]	M. Rajagopalan, S. Praveen Kumar, and R. Anuthama, <i>FP-LAPW Study of the Elastic Properties of Al₂X (X=Sc,Y,La,Lu)</i> , Phys. B Condens. Matter 405 , 1817 (2010).
[58]	S. F. Pugh, <i>XCII. Relations between the Elastic Moduli and the Plastic Properties of Polycrystalline Pure Metals</i> , J. Sci. 45 , 823 (1954).
[59]	A. Moussali, M. B. Amina, B. Fassi, I. Ameri, M. Ameri, and Y. Al-Douri, <i>First-Principles Calculations to Investigate Structural and Thermodynamic Properties of Ni₂LaZ (Z = As, Sb and Bi) Heusler Alloys</i> , Indian J. Phys. 94 , 1733 (2020).
[60]	G. Vaitheeswaran, V. Kanchana, A. Svane, and A. Delin, <i>Elastic Properties of MgCNi₃—a Superconducting Perovskite</i> , J. Phys.: Condens. Matter 19 , 326214 (2007).
[61]	B. Fadila, M. Ameri, D. Bensaid, M. Noureddine, I. Ameri, S. Mesbah, and Y. Al-Douri, <i>Structural, Magnetic, Electronic and Mechanical Properties of Full-Heusler Alloys Co₂YAl (Y = Fe, Ti): First Principles Calculations with Different Exchange-Correlation Potentials</i> , J. Magn. Magn. Mater. 448 , 208 (2018).
[62]	W. D. C. Jr and D. G. Rethwisch, <i>Fundamentals of Materials Science and Engineering: An Integrated Approach</i> (John Wiley & Sons, 2020).
[63]	H. Fu, D. Li, F. Peng, T. Gao, and X. Cheng, <i>Ab Initio Calculations of Elastic Constants and Thermodynamic Properties of NiAl under High Pressures</i> , Comput. Mat. Sci. 44 , 774 (2008).
[64]	J. Haines, J. Léger, and G. Bocquillon, <i>Synthesis and Design of Superhard Materials</i> , Annu. Rev. Mater. Res. 31 , 1 (2001).
[65]	L. Vitos, P. A. Korzhavyi, and B. Johansson, <i>Stainless Steel Optimization from Quantum Mechanical Calculations</i> , Nat. Mater. 2 , 1 (2003).

[66]	K. J. Puttlitz and K. A. Stalter, in <i>Handbook of Lead-Free Solder Technology for Microelectronic Assemblies</i> (Springer, New York, 2005), p. 95.
[67]	R. C. Lincoln, K. M. Koliwad, and P. B. Ghate, <i>Morse-Potential Evaluation of Second- and Third-Order Elastic Constants of Some Cubic Metals</i> , Phys. Rev. 157 , 463 (1967).
[68]	S.-H. Jhi, J. Ihm, S. G. Louie, and M. L. Cohen, <i>Electronic Mechanism of Hardness Enhancement in Transition-Metal Carbonitrides</i> , Nature 399 , 6732 (1999).
[69]	X.-Q. Chen, H. Niu, D. Li, and Y. Li, <i>Modeling Hardness of Polycrystalline Materials and Bulk Metallic Glasses</i> , Intermetallics 19 , 1275 (2011).
[70]	Y. Tian, B. Xu, and Z. Zhao, <i>Microscopic Theory of Hardness and Design of Novel Superhard Crystals</i> , Int. J. Refract. Met. Hard Mater. 33 , 93 (2012).
[71]	D. M. Teter, <i>Computational Alchemy: The Search for New Superhard Materials</i> , MRS Bull. 23 , 22 (1998).
[72]	N. Miao, B. Sa, J. Zhou, and Z. Sun, <i>Theoretical Investigation on the Transition-Metal Borides with Ta₃B₄-Type Structure: A Class of Hard and Refractory Materials</i> , Comput. Mater. Sci. 50 , 1559 (2011).
[73]	E. Mazhnik and A. R. Oganov, <i>A Model of Hardness and Fracture Toughness of Solids</i> , J. Appl. Phys. 126 , 125109 (2019).
[74]	H. Niu, S. Niu, and A. R. Oganov, <i>Simple and Accurate Model of Fracture Toughness of Solids</i> , J. Appl. Phys. 125 , 065105 (2019).
[75]	S. Yin et al., <i>Hardness and Elastic Moduli of High Pressure Synthesized MoB₂ and WB₂ Compacts</i> , High Press. Res. 33 , 409 (2013).
[76]	P. Ravindran, L. Fast, P. A. Korzhavyi, B. Johansson, J. Wills, and O. Eriksson, <i>Density Functional Theory for Calculation of Elastic Properties of Orthorhombic Crystals: Application to TiSi₂</i> , J. Appl. Phys. 84 , 4891 (1998).
[77]	X. Gao, Y. Jiang, R. Zhou, and J. Feng, <i>Stability and Elastic Properties of Y–C Binary Compounds Investigated by First Principles Calculations</i> , J. Alloys Compd. 587 , 819 (2014).
[78]	J. Wang, Y. Zhou, T. Liao, and Z. Lin, <i>First-Principles Prediction of Low Shear-Strain Resistance of Al₃BC₃: A Metal Borocarbide Containing Short Linear BC₂ Units</i> , Appl. Phys. Lett. 89 , 021917 (2006).

[79]	C. M. Kube and M. de Jong, <i>Elastic Constants of Polycrystals with Generally Anisotropic Crystals</i> , J. Appl. Phys. 120 , 165105 (2016).
[80]	V. Arsigny, P. Fillard, X. Pennec, and N. Ayache, <i>Fast and Simple Calculus on Tensors in the Log-Euclidean Framework</i> , in <i>Medical Image Computing and Computer-Assisted Intervention – MICCAI 2005</i> , Vol. 3749 (Springer, Berlin, Heidelberg, 2005), pp. 115–122.
[81]	C. M. Kube, <i>Elastic Anisotropy of Crystals</i> , AIP Adv. 6 , 095209 (2016).
[82]	S. I. Ranganathan and M. Ostoja-Starzewski, <i>Universal Elastic Anisotropy Index</i> , Phys. Rev. Lett. 101 , 055504 (2008).
[83]	Y. H. Duan, Y. Sun, M. J. Peng, and S. G. Zhou, <i>Anisotropic Elastic Properties of the Ca–Pb Compounds</i> , J. Alloys Compd. 595 , 14 (2014).
[84]	R. Gaillac, P. Pullumbi, and F.-X. Coudert, <i>ELATE: An Open-Source Online Application for Analysis and Visualization of Elastic Tensors</i> , J. Phys.: Condens. Matter 28 , (2016).
[85]	Md. S. Rana, R. Ahmed, Md. S. Islam, R. S. Islam, and S. H. Naqib, <i>DFT Based Investigation of Structural, Elastic, Optoelectronic, Thermophysical and Superconducting State Properties of Binary Mo₃P at Different Pressures</i> , Next Mater. 6 , 100284 (2025).
[86]	K. Boudiaf, A. Bouhemadou, Y. Al-Douri, R. Khenata, S. Bin-Omran, and N. Guechi, <i>Electronic and Thermoelectric Properties of the Layered BaFAgCh (Ch = S, Se and Te): First-Principles Study</i> , J. Alloys Compd. 759 , 32 (2018).
[87]	A. Bekhti-Siad, K. Bettine, D. P. Rai, Y. Al-Douri, X. Wang, R. Khenata, A. Bouhemadou, and C. H. Voon, <i>Electronic, Optical and Thermoelectric Investigations of Zintl Phase AE₃AlAs₃ (AE = Sr, Ba): First-Principles Calculations</i> , Chinese J. Phys. 56 , 870 (2018).
[88]	A. Belhachemi, H. Abid, Y. Al-Douri, M. Sehil, A. Bouhemadou, and M. Ameri, <i>First-Principles Calculations to Investigate the Structural, Electronic and Optical Properties of Zn_{1-x}Mg_xTe Ternary Alloys</i> , Chinese J. Phys. 55 , 1018 (2017).
[89]	A. H. Reshak and S. Auluck, <i>Theoretical Investigation of the Electronic and Optical Properties of ZrX₂ (X=S, Se and Te)</i> , Phys. B Condens. Matter 353 , 230 (2004).
[90]	J.-H. Xu, T. Oguchi, and A. J. Freeman, <i>Crystal Structure, Phase Stability, and Magnetism in Ni₃V</i> , Phys. Rev. B 35 , 6940 (1987).

[91]	E. Schreiber, O. L. Anderson, and N. Soga, <i>Elastic Constants and Their Measurement</i> (McGraw-Hill, New York, 1974).
[92]	M. F. Ashby, P. J. Ferreira, and D. L. Schodek, <i>Material Classes, Structure, and Properties</i> , in <i>Nanomaterials, Nanotechnologies and Design</i> (Elsevier, 2009), pp. 87–146.
[93]	J. R. Christman, <i>Fundamentals of Solid State Physics</i> (Wiley, New York, 1988).
[94]	O. L. Anderson, <i>A Simplified Method for Calculating the Debye Temperature from Elastic Constants</i> , <i>J. Phys. Chem. Solids</i> 24 , 909 (1963).
[95]	M. E. Fine, L. D. Brown, and H. L. Marcus, <i>Elastic Constants versus Melting Temperature in Metals</i> , <i>Scr. Metall.</i> 18 , 951 (1984).
[96]	D. Salamon, <i>Chapter 6 - Advanced Ceramics</i> , in <i>Advanced Ceramics for Dentistry</i> (Butterworth-Heinemann, Oxford, 2014), pp. 103–122.
[97]	M. A. Ali, M. M. Hossain, M. M. Uddin, A. K. M. A. Islam, and S. H. Naqib, <i>Understanding the Improvement of Thermo-Mechanical and Optical Properties of 212 MAX Phase Borides Zr_2AB_2 ($A = In, Tl$)</i> , <i>J. Mater. Res. Technol.</i> 15 , 2227 (2021).
[98]	D. R. Clarke, <i>Materials Selection Guidelines for Low Thermal Conductivity Thermal Barrier Coatings</i> , <i>Surf. Coat. Technol.</i> 163–164 , 67 (2003).
[99]	M. M. Hossain, M. A. Ali, M. M. Uddin, A. K. M. A. Islam, and S. H. Naqib, <i>Origin of High Hardness and Optoelectronic and Thermo-Physical Properties of Boron-Rich Compounds B_6X ($X = S, Se$): A Comprehensive Study via DFT Approach</i> , <i>J. Appl. Phys.</i> 129 , 175109 (2021).
[100]	G. A. Slack, <i>The Thermal Conductivity of Nonmetallic Crystals</i> , <i>Solid State Phys.</i> 34 , 1–71 (1979).
[101]	C. L. Julian, <i>Theory of Heat Conduction in Rare-Gas Crystals</i> , <i>Phys. Rev.</i> 137 , A128 (1965).
[102]	D. G. Cahill, S. K. Watson, and R. O. Pohl, <i>Lower Limit to the Thermal Conductivity of Disordered Crystals</i> , <i>Phys. Rev. B</i> 46 , 6131 (1992).
[103]	M. I. Naher and S. H. Naqib, <i>A Comprehensive Study of the Thermophysical and Optoelectronic Properties of Nb_2P_5 via Ab-Initio Technique</i> , <i>Results Phys.</i> 28 , 104623 (2021).
[104]	F. Parvin and S. H. Naqib, <i>Pressure Dependence of Structural, Elastic, Electronic, Thermodynamic, and Optical Properties of van Der Waals-Type $NaSn_2P_2$ Pnictide</i>

	<i>Superconductor: Insights from DFT Study</i> , Results Phys. 21 , 103848 (2021).
[105]	M. Roknuzzaman, M. Hadi, M. Abden, M. T. Nasir, A. K. M. Islam, M. Ali, K. Ostrikov, and S. H. Naqib, <i>Physical Properties of Predicted Ti_2CdN versus Existing Ti_2CdC MAX Phase: An Ab Initio Study</i> , Comput. Mater. Sci. 113 , 148 (2015).
[106]	M. A. Hadi, R. V. Vovk, and A. Chroneos, <i>Physical Properties of the Recently Discovered $Zr_2(Al_{1-x}Bi_x)C$ MAX Phases</i> , J. Mater. Sci.: Mater. Electron. 27 , 11925 (2016).
[107]	W. L. McMillan, <i>Transition Temperature of Strong-Coupled Superconductors</i> , Phys. Rev. 167 , 331 (1968).
[108]	Md. S. Islam, R. Ahmed, M. M. Hossain, M. A. Ali, M. M. Uddin, and S. H. Naqib, <i>Ab-Initio Insights into the Physical Properties of XIr_3 ($X = La, Th$) Superconductors: A Comparative Analysis</i> , Results Mater. 22 , 100568 (2024).
[109]	B. Rahman Rano, I. M. Syed, and S. H. Naqib, <i>Elastic, Electronic, Bonding, and Optical Properties of WTe_2 Weyl Semimetal: A Comparative Investigation with $MoTe_2$ from First Principles</i> , Results Phys. 19 , 103639 (2020).
[110]	A. K. M. A. Islam and S. H. Naqib, <i>Possible Explanation of High-T_c in Some 2D Cuprate Superconductors</i> , J. of Phys. Chem. Solids 58 , 1153 (1997).
[111]	S. Ram, V. Kanchana, G. Vaitheeswaran, A. Svane, S. B. Dugdale, and N. E. Christensen, <i>Electronic topological transition in $LaSn_3$ under pressure</i> , Phys. Rev. B 85 , 174531 (2012).
[112]	Z. Lin, L. V. Zhigilei, and V. Celli, <i>Electron-phonon coupling and electron heat capacity of metals under conditions of strong electron-phonon nonequilibrium</i> , Phys. Rev. B 77 , 075133 (2008).
[113]	J. Islam, S. K. Mitro, M. M. Hossain, M. M. Uddin, N. Jahan, A. K. M. A. Islam, S. H. Naqib, and M. A. Ali, <i>Exploration of the physical properties of the newly synthesized kagome superconductor $LaIr_3Ga_2$ using different exchange-correlation functionals</i> , Phys. Chem. Chem. Phys. 24 , 29640 (2022).
[114]	Z. Guguchia et al., <i>Tunable anomalous Hall conductivity through volume-wise magnetic competition in a topological kagome magnet</i> , Nat. Commun. 11 , 1 (2020).
[115]	C. Pei et al., <i>Pressure Induced Superconductivity in WB_2 and ReB_2 through Modifying the B Layers</i> , Sci. China Phys. Mech. Astron. 65 , 287412 (2022).